How non-conventional machining affects the surface integrity and magnetic properties of non-oriented electrical steel

Kieran Winter [a], Zhirong Liao [a,*], Ramkumar Ramanathan [b], Dragos Axinte [a], Gaurang Vakil [b], Christopher Gerada [b]

[a] Rolls-Royce UTC in Manufacturing and On-wing Technology, Faculty of Engineering, University of Nottingham, Nottingham NG7 2RD, UK
[b] Department of Electrical and Electronic Engineering, Faculty of Engineering, University of Nottingham, Nottingham NG7 2RD, UK

HIGHLIGHTS

- Machining causes magnetic deterioration in non-oriented electrical steels.
- Induced sub-granular misorientations act as pinning sites for magnetic domains.
- Magnetic domains may become disordered near to the machined edge.
- Abrasive waterjet cutting was found to minimally deteriorate the magnetic properties.

GRAPHICAL ABSTRACT
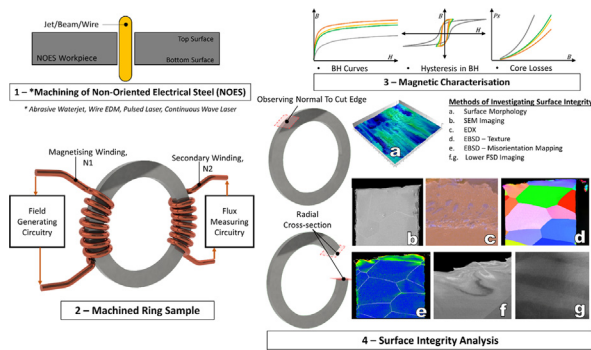
ARTICLE INFO

ABSTRACT

Non-oriented electrical steel (NOES) laminations are commonly used to manufacture the rotor and stator core of electric machines. To achieve high machine efficiencies, it is desirable for these NOES laminations to be able to achieve a high saturation magnetisation whilst incurring minimal core losses. It is known that inappropriate machining of these laminations could cause significant deterioration in their magnetic properties. However, the mechanisms by which machining influences this deterioration are less understood. This study investigates the magnetic deterioration after four nonconventional machining methods: Abrasive Waterjet, Wire Electric Discharge Machining, Pulsed Laser, and Continuous Wave Laser. An in-depth investigation of surface integrity through a range of methods, i.e., surface topography, scanning electron microscopy (SEM), nanoindentation, electron backscatter diffraction (EBSD), and magnetic domain imaging, were conducted to study the mechanisms causing magnetic deterioration. The surface integrity after machining using conventional methods (e.g., microstructure and texture), was found to not be of high relevance unless this is combined with analysis on how machining affects the micro-magnetic domain structure. This paper, for the first time, highlights this aspect and attempts to make initial quantitative evaluations on how the magnetic domains are affected in the superficial layer that is the result of non-conventional machining.

1. Introduction

In the search for ever-increasing electric machine efficiencies, intensive research is required to optimise all the processes

* Corresponding author.
E-mail address: Zhirong.Liao@nottingham.ac.uk (Z. Liao).

involved in its production so that electric propulsion can be commercially competitive on a global scale [1]. Electric propulsion can be achieved using a range of machine types such as: an induction machine; interior permanent magnet synchronous machines; synchronous reluctance machines etc. These machines can achieve high power densities and efficiencies, in which the successive energising and de-energising of the stator poles redirects the magnetic flux causing rotor progression [2]. The rapidly changing polarity requires materials that can be quickly and efficiently magnetised and de-magnetised, i.e., soft magnetic materials [3]. The ideal characteristics of a soft magnetic material for use in an electric motor are: high saturation magnetisation, high permeability, low core losses, and high resistivity. These characteristics can be summarised through the hysteresis behaviour in the magnetisation curve, where a tall, narrow loop is desirable [4].

Non-oriented electrical steels (NOES) are used as the motor application requires the material to behave magnetically isotropic. Therefore, regarding crystallographic texture, it is desirable to inhibit the proportion of crystal grains in the plane of the magnetic flux that are oriented with the 'hard' axis ($\langle 1\,1\,1 \rangle$ axis) of magnetisation during machining of the NOES sheets [5].

On the other hand, the electrical steel is normally supplied in sheets, which must be machined in order to produce the designed stator or rotor geometry, e.g., the numerous slots in the rotor laminations. The machining method chosen will have an influence on the microstructure at the cut edge which, in-turn, will be characterised as a difference in magnetic properties when compared to the supplier datasheet [6]. Previous studies have highlighted the deterioration of the BH characteristics (where B is the measured magnetic flux density and H is the applied magnetisation) and specific core losses of the material observed after machining compared to the raw soft magnetic materials [7]: (i) a large increase in specific core loss, where a 23.5% increase was measured in the machined stator core compared with the supplier material data; (ii) a significant reduction in magnetic saturation, causing a 0.8% reduction in the output torque of the assembled machine. This demonstrates the issue at hand which is, machining of a material and the corresponding surface integrity characteristics has a strong influence on the efficiency of electrical machines. In general, the NOES can be cut through conventional methods, i.e., punching, and non-conventional methods, e.g., Abrasive Waterjet (AWJ) [8,9], Wire Electric Discharge Machining (EDM) [10,11], and Laser cutting [12,13]. Among these methods, punching is the standard commercial process used in the manufacture of motor laminations due to the low cost, and it has been studied extensively. Research of the punching process, for example, has demonstrated the links between core losses and droop height, i.e., the plastically deformed material observed at the beginning of the cut, prior to the sheared surface [14], which is influenced by the material hardness and thickness. The implication of this study is that introducing plastic deformation at the cut edges results in the degradation of the magnetic performance of the material. Harstick et al., also highlighted the magnetic degradation due to the presence of plastic deformation at the cut edges of NOES sheets and further discusses the importance that localisation has on the magnetic performance [15]. They came to the expected conclusion that cutting with a sharp edge (reduced plastic deformation) is preferable over cutting with a blunt edge, i.e., deeper plastic deformation. As the material removal process is primarily achieved through shearing, the surface integrity effect of increased plastic deformation is mainly caused mechanically, with some thermal effects also present that caused by friction between the punch and the workpiece [15]. However, the mechanisms that caused the mechanical and thermal effects to negatively influence the magnetic performances were not investigated further with micro-magnetic analyses.

To overcome the severe mechanical defects associated with a physical/defined cutting edge, laser cutting could be considered. In contrast to mechanical punching, material hardness is no concern in laser processes [16]. Whilst laser processes have minimal mechanical effects, those induced thermally are introduced to the material at the cutting edge instead, i.e., tensile residual stresses [17,18]. The high amount of heat energy supplied by the laser is especially important in thin workpieces where the heat is dissipated through a greater volume than only the sub-surface [19]. This introduces significant thermal defects such as: residual thermal stresses, a Heat Affected Zone (HAZ), microcracks, and warping [17,20,21], which can significantly degrade the magnetic properties [20,22]. Another cutting process with thermal effects is Electro-Discharge-Machining (EDM), through which the thin NOES can be cut by high frequency electrical discharges that remove material by both vaporisation and melting [23]. The thermal effects associated with the high temperatures, like in the laser processes, are expected but these are expected to occur a much more localised manner beneath the cut edge [24]. Therefore, it is desirable to find a process that avoids the thermal effects observed in laser and EDM, which also avoids the large amount of plastic deformation that punching (mechanical cutting with a defined edge) causes.

For these requirements, Abrasive Waterjet (AWJ) cutting could be considered, which removes the material by directing a high velocity jet of water that is mixed with abrasive particles at the workpiece [25]. Although AWJ uses slow cutting speeds in comparison with the conventional punching method, potentially leading to higher production costs, there is commercial viability for low-volume applications (e.g., prototyping) where the punching tool costs may be avoided. AWJ is expected to affect the surface integrity of the workpiece less than when using a defined cutting edge (punching) as there is no physical cutting edge that can become worn, which could introduce a higher proportion of plastic deformation into the workpiece [26]. AWJ also has lower individual cutting forces, inducing fewer mechanical effects into the material [27], while it is also expected to have no such thermal defects found in laser and EDM as the waterjet acts as a coolant [28]. Due to these reductions in surface integrity defects after machining using AWJ cutting, it is expected that samples generated using this method will exhibit superior magnetic properties [29].

On the other hand, regardless of the different cutting methods, it is difficult to directly measure the magnetic properties of the cut edge on a micro or nanoscale after machining. Therefore, most of the current research focuses on the macro magnetic properties characterisation, e.g., by obtaining DC BH (magnetisation) curves, hysteresis loops, or core loss measurements for the whole sample, and then linking them with the cutting parameters. These results are used to optimise the cutting parameters through a series of cutting tests and magnetic measurements in an iterative methodology whilst lacking an in-depth understanding of the inherent influence that the stress conditions imparted to the NOES during machining has on the micro-magnetic properties directly beneath the cut edge.

As such, this paper investigates both the micro and macro scale surface integrity after non-conventional machining, and the magnetic performance of the non-oriented electrical steel (NOES) for an identical cut geometry, to reveal, for the first time, the mechanisms of magnetic deterioration when machining induced defects are introduced for different machining methods. For this, four non-conventional machining methods: Abrasive Waterjet (AWJ), Wire Electric Discharge Machining (EDM), Pulsed Laser (PL), and Continuous Wave Laser (CW), have been investigated. This contrasts with much of the current research in the field which tends to focus on the optimisation of one specific process. The in-depth analysis of machining induced surface integrity was conducted

through 3D surface topography, SEM, EBSD and nanoindentation analyses. Furthermore, for the first time both the macro level, i.e., BH characteristics and core loss performance, and micro level, i.e., magnetic domain structure at the cutting edge, have been investigated to reveal the mechanisms of the magnetic deterioration. Magnetic domains are regions in the ferromagnetic material where spontaneous magnetisation to the saturation point exists, but, in order to remain in a demagnetised state, the directions of these magnetisation vectors are such that there is no predominant magnetisation for the entire sample. Where the magnetisation direction changes, boundaries can be observed, these are referred to as domain walls. As such, observing these allow for the fundamental investigation into how surface integrity influences the magnetic performance through modification of the static magnetic domain structure, whereby the domain wall motion can be inhibited when the applied field direction changes through motor progression. Thus, the defects can be compared on a common scale, enabling a valid relative comparison of each process. This will enable the investigation of the effect of machining methods on the electrical properties of NOES and the mechanisms by which surface integrity affects these.

2. Methodology

The material investigated is non-oriented electrical steel (NOES) containing 2.4 wt% Si. Ring samples of single sheets with the dimensions 32 mm × 24 mm × 0.2 mm (OD × ID × Thickness) were cut using each of the tested cutting methods: Continuous Wave Laser (CW), Pulsed Laser (PL), Wire Electro Discharge Machining (EDM), and Abrasive Waterjet Machining (AWJ) using the cutting parameters specified in Table 1. These parameters were pre-optimised for the material prior to producing the samples for the magnetic investigations.

CW, PL and EDM were studied to investigate the influence of the thermal effect localisation, while AWJ was employed to investigate the influence of the mechanical effects in the absence of a fixed cutting edge.

To magnetically characterise the material, data was collected following the IEC 60404–4 standard to test ring samples [30]. Known as the *ring method* (Fig. 1b), the sample is a toroid of NOES with a rectangular cross-section. Wound tightly around the ring sample are two windings: (N1) The *magnetising winding* – which is responsible for applying the *external magnetic field*, and (N2) the *secondary winding* – which is used in the measurement of the induced magnetic flux density. Two experiment runs for each sample were completed: (1) Measuring the magnetic flux density, B, (T) as the magnetic field strength, H, (A/m) was increased. When plotted, this enabled the comparison of the magnetisation (BH) curves

for the samples from each process. (2) Evaluation of the specific iron loss, P_S, (W/kg) as H was increased for various flux densities and frequencies. This loss is comprised from both the eddy current and hysteresis losses.

The ring dimensions chosen were small as to amplify the effect of machining's influence on the magnetic behaviour of the workpiece as, the HAZ for example, will affect a larger proportion of the cross-section. This amplification of the effects of machining aided in comparing the processes with the analytical techniques used. The results for the specific iron losses and the hysteresis loops corresponding to a frequency of 500 Hz are presented in this paper to be representative of the operating conditions present of high-performance electrical machines.

After cutting, to prepare the samples for microscopy and nanoindentation, they were cross-sectioned, hot mounted in conductive Polyfast resin, then plane ground and subsequently polished using 0.06 μm colloidal silica.

The samples were etched using a 5% Nital solution to reveal the grain structure, and Scanning Electron Microscope (FEI Quanta600 SEM) micrographs were produced for each of the machining processes. The Electron Backscatter Diffraction (EBSD) data was acquired using the JEOL 7100F FEG-SEM where the sample was tilted at 70° and an accelerating voltage of 15 kV was applied. For the investigating the magnetic domain structure beneath the cut surface, a high accelerating voltage (30 kV) and beam current (10 μA) was used to increase the type-2 magnetic contrast [31] under the Forward Scatter Detector (FSD). Type-2 magnetic contrast arises when the paths of backscattered electrons are shifted by the internal magnetic fields caused by the magnetic domains within the sample. The effect of either attraction or repulsion on the backscattered electrons leads to the formation of image contrast caused by the magnetic domains [32]. This enables the fundamental investigation of the machining induced magnetic deterioration mechanisms, whereby the modification of the magnetic domain structure can be revealed and correlated with the surface defects.

Surface topography data was collected using the Bruker-Alicona InfiniteFocus 3D surface measurement system with a 100x magnification and the map area of 200 μm X 200 μm. The data was processed using Digital Surf's MountainsMap Premium, which allowed for non-destructive analysis on a 3D digital replica of the cut surface through the production of topography gradient maps.

To investigate any changes in hardness as a function of distance from the cut edge, nanoindentation measurements were collected using a Berkovich tip. A load of 25 mN was applied at a rate of 2.25 mNs^{-1} with a dwell period of 5 s at the peak load. The hardness at each indentation point was then determined using an Oliver and Pharr analysis [33]. 20 indentations with a vertical spacing of

Table 1
Cutting process parameters employed to produce the ring samples used for both magnetic characterisation and material analysis.

Method	Parameter	Value
Abrasive Waterjet (AWJ)	Pump pressure (Bar)	3000
	Abrasive flow rate (g/min)	80
	Cutting speed (mm/min)	140
Wire Electrical Discharge Machining (EDM)	Wire diameter (mm)	0.25
	Wire material	Brass
	Cutting speed (mm/min)	12
	Power (W)	63
Pulsed Laser (PL)	Power (W)	17
	Cutting speed (mm/min)	500
	Pulse width (ns)	200
	Pulse frequency (kHz)	35
	Repetitions	350
Continuous Wave (CW) Laser	Power (W)	1000
	Cutting speed (mm/min)	3000
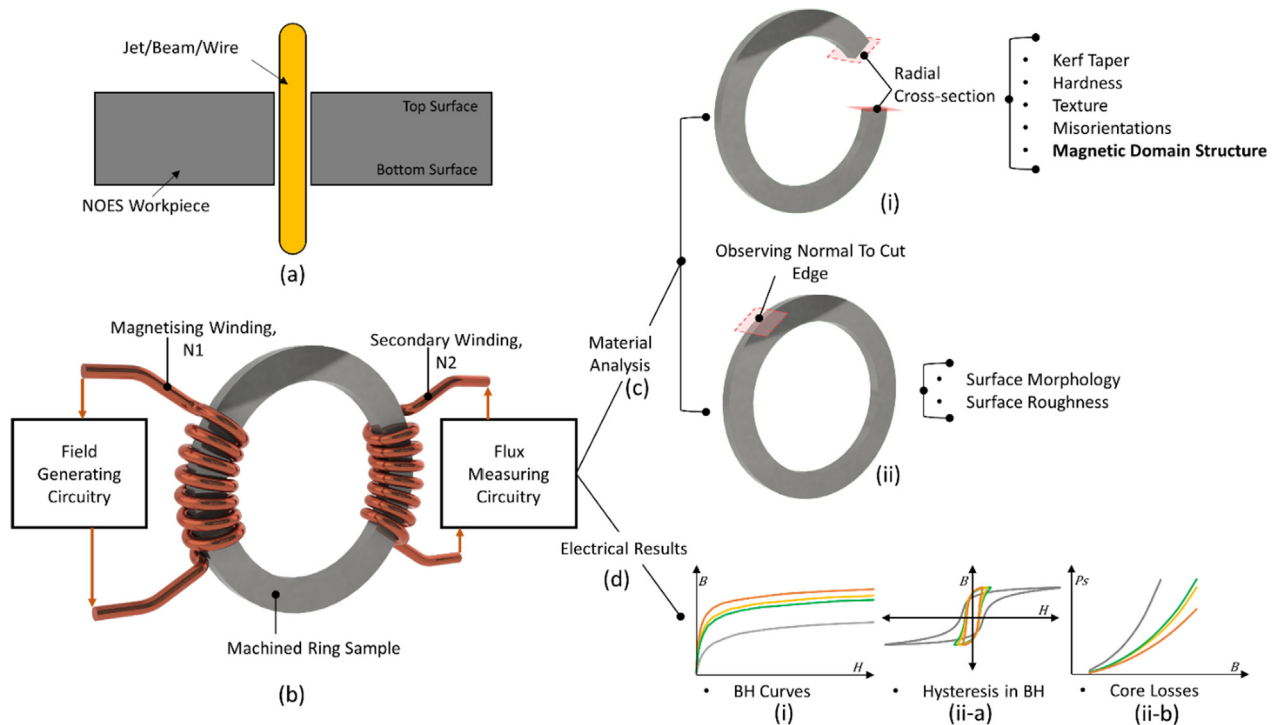
Fig. 1. Cross-section diagram showing the jet/beam/wire cutting the samples used for the subsequent analyses (a). Schematics representing the machined ring sample and windings used for magnetic characterisation to the IEC 60404–4 standard (b), the areas of the machined ring samples that have been selected for material/surface analysis. This is by investigating a radial cross-section (c-i) and normal to the cut edge (c-ii). The magnetic properties after machining are collected through the experimental setup in (b), these are: BH curves (d-i), hysteresis in BH loops (d-ii-a), and the associated core losses (d-ii-b) - where the deviations exist due to the combined effects observed in (c).

5 μm were used to plot the hardness as distance beneath the cut surface increased.

3. Results and discussion

3.1. Magnetic characterisation of the NOES sheets after machining

A key performance indicator of soft magnetic materials used in electric machines is the ability to achieve a high saturation magnetisation at a low applied field strength. The BH curves (Fig. 2a) obtained after machining the samples indicate that AWJ allows for the highest saturation to be achieved (B = 1.0 T). By contrast, CW achieved the lowest saturation magnetisation (B = 0.5 T), and the EDM and PL samples exhibited similar BH behaviour to each other. This would indicate that in the AWJ sample, there is a greater proportion of magnetic domains that have the ability to become aligned with the direction of the applied field compared to the others – enabling a higher induced magnetisation.

Following the same trend, the specific iron loss curves (Fig. 2b) obtained after machining indicate how the lowest losses occur in samples cut with AWJ (P_s = 7.4 W/kg at 500 Hz and 0.5 T), which is 36% of CW that was found to have the highest (P_s = 20.6 W/kg at 500 Hz and 0.5 T) . The EDM and PL samples exhibited similar loss behaviour (P_s = 9.3 W/kg and 10.1 W/kg respectively at 500 Hz and 0.5 T). In comparing the losses for AWJ and CW, which when generalised as a key performance indicator for a motor, there is the implication that large improvements in electrical efficiency could be achieved by selecting AWJ over CW for cutting the NOES laminations. As the core losses are comprised of both those due to eddy currents and the hysteresis behaviour in BH, where the former is largely controlled by material thickness, the latter requires further investigation to understand if there is a change in coercive force after machining the samples.

The investigate if the disparity in P_S is due to alterations in the BH hysteresis characteristics, the hysteresis loops were plotted (Fig. 2c). By comparing the shapes of the hysteresis loops, the CW loop width is wide – indicative of higher coercive force to overcome in order to achieve magnetic saturation. This is contrasted by the considerably thinner AWJ loop width – indicative of a lower coercivity which in turn, translates to a lower electrical energy expenditure in reversing the applied magnetic field direction leading to the lower core losses.

These results demonstrate how there is a significant variation in the magnetic properties of the NOES laminations after non-conventional machining – where the extent of the deterioration is dependent upon the machining method selected. For this investigation, AWJ is the superior method in terms of achieving desirable magnetic characteristics and cutting by CW is the worst.

To explore the disparity observed in Fig. 2, the difference in saturation (Fig. 2a) could lead to the assumption that in the sample cut by CW, there will be a severe increase in magnetic reluctance, $\mathcal{R}$, (H^{-1}) (1) (the opposition to magnetic flux, comparable to the concept of electrical resistance), caused by a combination of the geometric and metallurgical changes induced by machining. This assumption can be made from the definition of $\mathcal{R}$ which can be calculated in a uniform magnetic circuit by:

$$\mathcal{R} = \frac{l}{\mu A} \tag{1}$$

where: l is the circuit length (m), μ is the permeability of the material, and A is the cross-sectional area (m^2). Here it is clear that for a constant circuit length, $\mathcal{R} \propto (\mu A)^{-1}$, therefore any reduction in both: (1) μ, e.g., through surface defects including the presence of residual stresses, morphological defects, metallurgical and crystallographic defects, and (2) geometrical changes, A, i.e., through kerf tapering would present as a reduction in magnetic saturation observed in
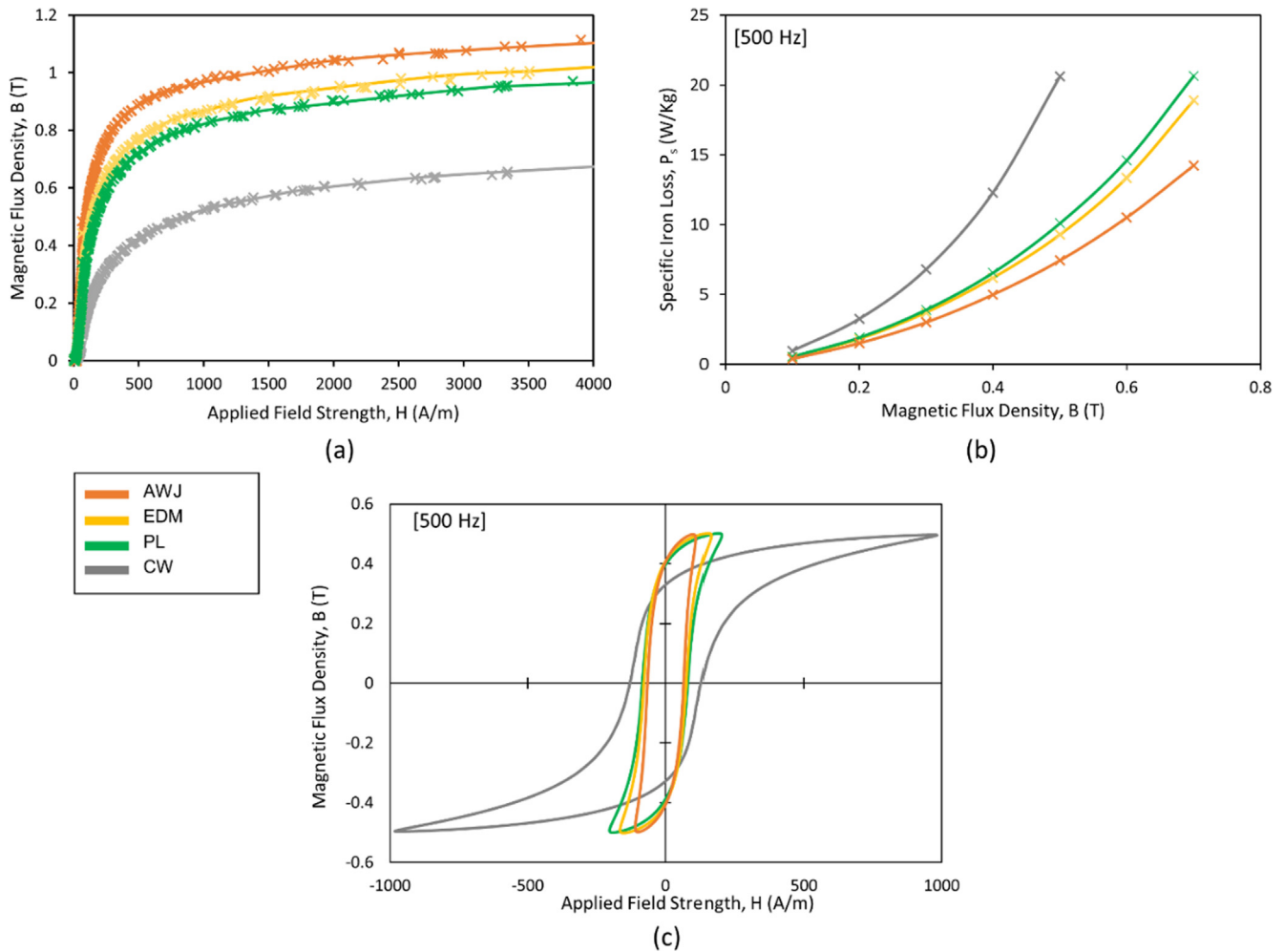
Fig. 2. The macro-magnetic data for samples after experiencing machining by all of the investigated processes – consisting of: the BH curves (a), Specific Iron loss (Ps) curves (measured at 500 Hz) (b), and Hysteresis curves (Measured at 500 Hz to 0.5 T) (c).

the BH curves. Generalising this result into a practical scenario, with the saturation magnetisation also having a strong influence on the achievable power densities of a motor, a 50% difference arising exclusively from choice of machining method makes it evident that research into the deterioration mechanisms causing this inconsistency in magnetic performance is vital in order to inform future process optimisation decisions.

In the context of manufacturing core laminations for electrical motors, which are expected to have a greater total length of machined edges compared to the toroidal samples, the effects of machining can be compounded. It becomes clear that to develop more efficient electrical machines, the choice of machining method becomes a crucial factor for the designer to consider. To provide rationale to support making these decisions, it is imperative to not-only acknowledge the observable difference in the magnetic performance of NOES after various machining methods, but to also understand the role that machining induced surface integrity defects have in influencing the micro-magnetic material properties.

3.2. Surface morphology of NOES sheets after machining

In order to further understand the mechanisms by which the effects of machining deteriorate the magnetic properties of the NOES laminations, a range of surface integrity analyses have been

performed. The macro-scale features present on the cut surfaces (Fig. 3) are all within expectations for the machining of a relatively ductile steel by the various methods (i.e., scratches in AWJ (Fig. 3a), a proportion of recast material in the thermal processes – EDM (Fig. 3b), PL (Fig. 3c), CW (Fig. 3d)), as such, the analyses are used to indicate the scale of deformation and to abstractly posit the sources of residual stresses in the sub-surface layers.

The change in areal surface roughness (Fig. 3) shows a correlation with the order of magnetic deterioration, considering Ampere's law for the magnetic flux density, B, in a toroidal sample with applied current, I, N number of turns, permeability, μ, and radius, r:

$$B = \frac{\mu NI}{2\pi r} \tag{2}$$

The variation in S_a could be considered to influence the value of r. This yields a small decrease of 0.02% from max r_{CW} to min r_{AWJ}, although, from the ISO 60404–4 standard (23) used for the magnetic characterisation, the maximum acceptable uncertainty in both measurements D and d is $\pm 0.25\%$ or better. Therefore, the deviations in r caused by the different S_a values fall within the allowable variation for the test method and cannot alone account for the 50% change in B observed (Fig. 2a). This leads to the assumption that changes in μ throughout the material hold a greater weighting when influencing the magnetic flux density.
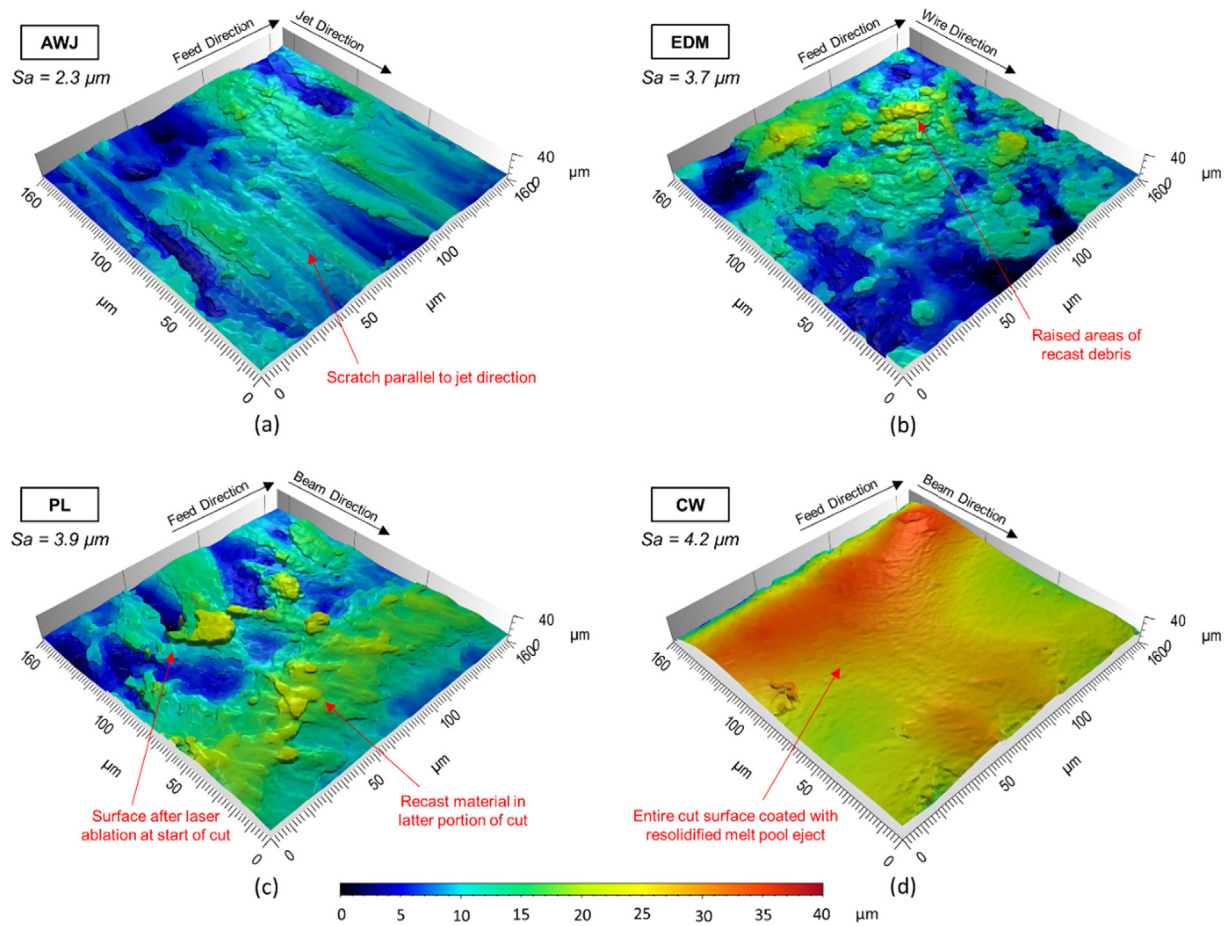
Fig. 3. Surface topography maps observing the cut surface for samples machined by abrasive waterjet, wire EDM, pulsed laser, and continuous wave laser. - highlighting the macro-level features present – indicating the sources of the machining stresses.

The results from the surface topography analysis reveal macro-level insights into the characteristic features of each cutting method studied. Whilst there is a correlation between the S_a values and the level of deterioration in magnetic properties, this does not explain the fundamental mechanisms causing it. Hence further investigation beneath the cut surface is required in order to fully explain the causes of magnetic deterioration after machining.

3.3. Microstructural investigations of the machined profiles of the NOES sheets

To further investigate the causes of deterioration in the magnetic properties, SEM micrographs observing a cross-section view of each cut surface were produced (Fig. 4). The samples were etched to determine if there was any visible change in microstructure after machining.

Due to the nature of mechanical material removal in AWJ and the thin thickness of the NOES sheet, a burr is visible at the exit of the cut (Fig. 4a). This has the potential to damage the neighbouring laminations when assembled by scratching the insulating coating, causing short circuits. This would also decrease the resistivity of the assembled core and thus, increase Eddy losses. Moreover, a taper of 4.2° is measured due to the defocus of waterjet plume as distance increases from the nozzle. This kerf taper effect in AWJ can however be reduced through process optimisation techniques such as reducing the standoff distance or reducing the jet traverse speed (increasing cutting times) [34].

Unlike the beam processes, for the sample cut by EDM (Fig. 4b) there is no taper as expected, as the wire is of a constant diameter throughout the depth of cut. This means that samples cut by EDM give the best possibility of achieving a perpendicular cut, i.e., good geometrical accuracy to the intended design. However, a discontinuous recast layer due to the sub-optimal removal of the eroded debris by water flushing has been observed. The crystal structure of the recast material is not controlled when compared to the desirable base material. Similar to the EDM sample, a recast layer is observed at the cut edge of PL sample (Fig. 4c), although it is continuous due to melting occurring as well as ablation. Moreover, there is a linear taper of 11.3° observed, which can be attributed to the beam defocus through the depth of the cut – reducing the energy intensity as the beam diverges. The sample cut by CW (Fig. 4) exhibits the lowest geometrical accuracy, where an ideal cut profile would be perpendicular to the entry and exit surfaces of the lamination. There is a line visible that marks where the ejected melt pool spatter has coated the cut surface and resolidified. Due to the behaviour of the melt pool spatter, this taper inverse and non-linear, with a maximum measured angle of 31.1°.

Concerning the samples with a tapered cut edge (Fig. 5a), although the windings are wound tightly, there will be a discontinuous air gap which the magnetic flux will have to traverse prior to entering the sample. This is contrasted by the samples with a perpendicular cut (Fig. 5b) where the air gap is a constant distance. Recalling (1), how $\mathcal{R} \propto l(\mu A)^{-1}$, if the air gap is considered to be a medium where $\mu = \mu_0$ (vacuum permeability), then increasing
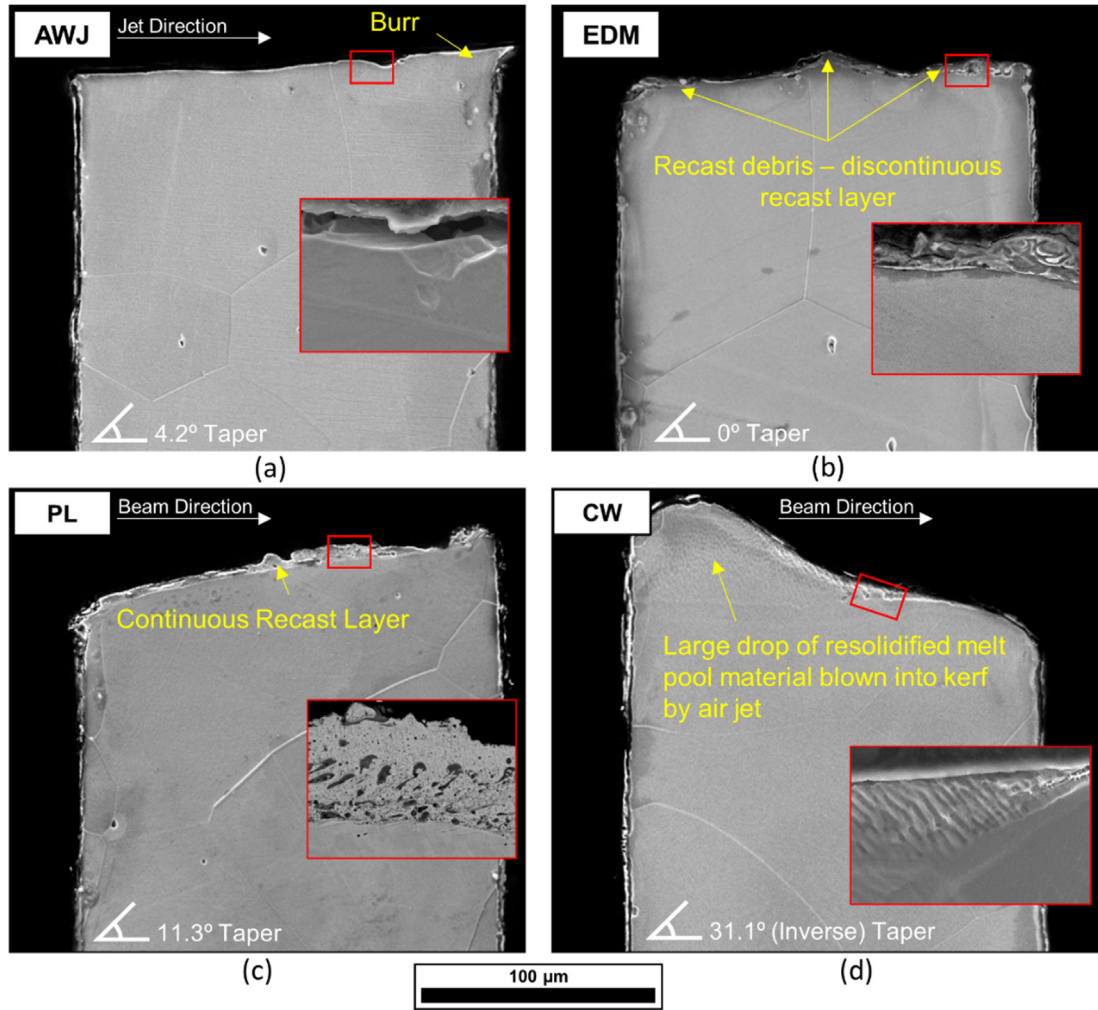
Fig. 4. SEM micrographs observing a cross-section view of the samples for samples machined by abrasive waterjet, wire EDM, pulsed laser, and continuous wave laser. The samples have been etched to reveal the grain boundaries.
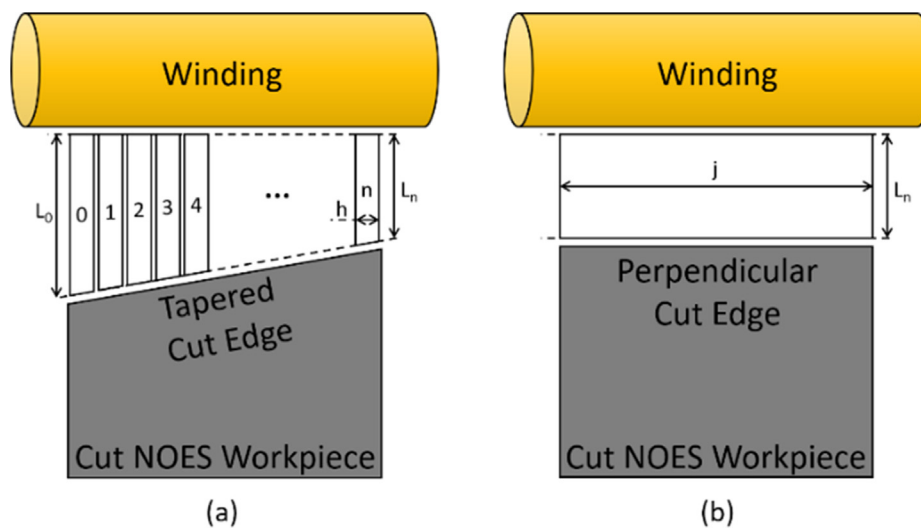
Fig. 5. Schematic showing the variation in l in the airgap for a tapered cut edge (a) compared with that of a perpendicular cut edge (b).

the width of the area of relatively low permeability that the flux needs to traverse due to the taper increases the reluctance. By dividing the air gap into small segments (Fig. 5a) of width, h, length, l, and thickness, t, then the reluctance across the tapered air gap can be approximated as the summation of the individual air gap reluctances in parallel:

$$\frac{1}{\mathcal{R}_{Taper}} \sum_{i=1}^{n} \left(\frac{l_n}{\mu_0 ht}\right)^{-1} \tag{3}$$

Whereas the reluctance across the perpendicular air gap with whole sample width, $j = nh$, (Fig. 5b) can be considered:

$$\mathcal{R}_{Perpendicular} = \frac{l_n}{\mu_0 jt} \tag{4}$$

Therefore, $\mathcal{R}_{Taper} > \mathcal{R}_{Perpendicular}$ for a common material and sample width, j, as the magnetic flux would be required to cross a larger air gap which has a reduced permeability.

If the magnetic flux were to travel perpendicularly across the air gap from the wire, an increased reluctance would be observed due to the taper. In practice, this is an oversimplified approach – as the magnetic flux travels the path of least reluctance, it will favour the shorter air gap distance, not making full use of the available magnetic material and reducing the saturation. Also, if the effects of edge taper on magnetic performance were weighted highly, the sample cut by EDM would be expected to surpass AWJ, yet it achieves similar results to the sample cut by PL. This leads to the assumption that a change in μ beneath the cut edge in the workpiece itself is the larger factor influencing magnetic performance.

In soft magnetic materials, μ varies with both H (Fig. 6a) and with material structure [3], therefore, as H is controlled during magnetic characterisation, changes in μ occur due to the latter. This assertion is strengthened when observing the BH behaviour in a low (0–80 A/m) applied field (Fig. 6b) where Barkhausen jumps exist in all of the samples in the common region of H (60–70 A/m). The Barkhausen jumps mark the transition from where the magnetisation mechanism changes from total domain wall motion (requiring low H values) to a combination that also includes domain wall rotation (requiring higher H values) [35]. As the domain walls are located in such a way to minimise the system energy (i.e., magnetostatic energy and magnetoelastic energy) [3], any hindrances to their optimum alignment with a crystallographic easy axis will require a greater proportion of the magnetisation to occur by rotation as opposed to motion – requiring more energy to produce the higher H values. In comparing the AWJ and CW samples, the higher value of B achieved in AWJ prior to the Barkhausen jump indicates that a greater volume of the material is susceptible to domain wall motion, whereas in CW, some hindrances to domain wall motion exist – inhibiting the growth of B. Hence, the assumption that the main factor influencing the magnetic deterioration comes from the crystallographic changes

beneath the machined surface as opposed to the small-scale changes to the edge geometry stands.

Previous studies that have compared the macro-magnetic properties of machined samples with those that have undergone stress relief annealing highlight the influence of residual stresses on the BH and hysteresis performance, specifically, that a reduction is desirable [35]. Further to this, magnetic Barkhausen noise has been used to non-destructively measure residual stresses in ferromagnetic parts [36,37]. Therefore, it is expected that an increase in residual stresses induced by machining will directly correlate with the deterioration in the magnetic performance. To investigate if localisation of the induced stresses after machining causes the domain wall interactions, nanoindentation was performed to identify if there is a variation in hardness as distance increases from the cut edge (Fig. 7). This enables the indirect measurement of the localisation of the stresses.

As expected, the AWJ sample shows an increased hardness at the cut edge, this is an increase of 13.3% due to the work hardening effect induced by mechanical impact of the abrasives, while this value smoothly decreases to a linear value of 2.6 GPa after 40 μm, i.e., the hardness of the base material. However, in contrast to the work hardening effect in AWJ cutting, the hardness changes observed after the thermal processes, i.e., EDM, PL and CW cutting, could be attributed to the over-ageing effect that occurs under high temperatures. Specifically, the hardness of the EDM cut sample is increased in by a maximum of 30.4% at the cut edge which rapidly decreases to a linear value of 2.6 GPa after 15 μm. At the PL cut edge, there was an increase in hardness of 13.3% which decreases with a shallow gradient to a linear value of 2.6 GPa after 80 μm. The hardness of the CW cut sample increased by a much greater magnitude when compared with PL, i.e., by a maximum of 22.7% at the cut edge and it did not decrease to the linear value of 2.6 GPa over the measured distance, i.e., 100 μm. This is due to the ubiquitous heat penetration that causes a significant over-ageing effect throughout a great depth in the very-thin NOES sheet.

More interestingly, for the thermal processes (EDM, PL, CW), the rate at which the hardness returns to the baseline value correlates with the deterioration in magnetic properties (Fig. 2). This implies that the more localised the thermally induced change in hardness after machining, the lesser the deterioration in magnetic properties. For the sample cut by AWJ, despite having an equal increase in hardness as PL and a lower rate of return than EDM, it experiences less magnetic deterioration.

From these measured changes in hardness (and the implied greater induced stresses from machining), the variation in perme-
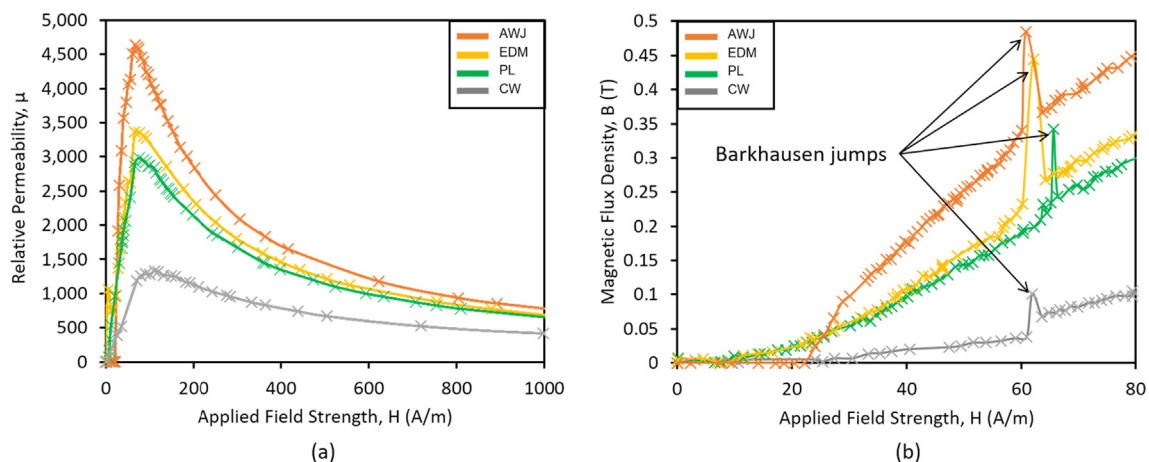
Fig. 6. Relative permeability, μ, curves as H is increased (a) and the BH behaviour in a low applied field (b) for samples machined by abrasive waterjet, wire EDM, pulsed laser, and continuous wave laser.
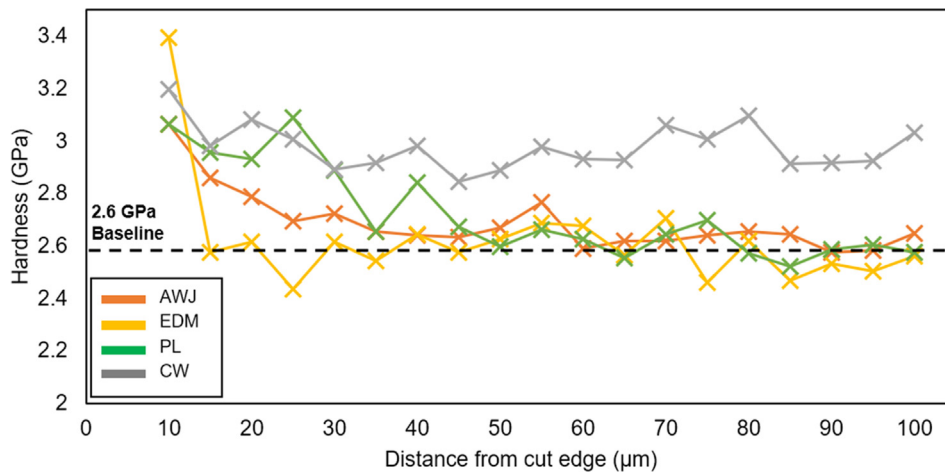
Fig. 7. Nanoindentation measurement of hardness as distance increases from the cut edge for samples machined by abrasive waterjet, wire EDM, pulsed laser, and continuous wave laser.

ability across the sample width, y, can be considered as being dependent on the distance, x, away from the cut edge where there is a gradient in permeability (Fig. 8). Evaluating this gradient as discrete zones of degraded material and base material for a line segment of the toroid gives:

$$\bar{\mu}_{Sample} = \frac{2x\mu_{Degraded} + (y - 2x)\mu_{Base}}{y} \tag{6}$$

where the mean permeability is dependent on both the permeability of the degraded zone and the depth that this extends into the base material.

To investigate whether this degradation in μ occurs due to a change in the crystallographic texture after machining, EBSD was used to produce inverse pole figure (IPF) maps. EBSD data was also used to study a number of other crystallographic parameters retroactively [38]. These secondary parameters have allowed for the identification of substructures within the grains near the cutting edges that indicate these areas are stress affected or have undergone recrystallisation.

In the IPF maps (Fig. 9), an area with a colour gradient (a local change in the crystallographic orientations) indicates an area that has been stress affected, such as the mechanical stress that is imparted to the workpiece after AWJ. It can also indicate recrystallisation in the HAZ in the thermal processes, i.e., in the EDM sample.

Fig. 8. Plan view schematic of the toroidal sample with zones of decreased permeability near the cut edge.

In the sample cut by AWJ (Fig. 9a), a gradient is observed along the cut edge. This indicates that there is a level of deformation introduced mechanically during machining. The mixed orientations observed in the burr – which takes on much of the stress supports this, i.e., mechanically induced recrystallisation. In the sample cut by EDM (Fig. 9b), the mixed orientations observed in the recast debris indicates thermally induced recrystallisation, but this does not visibly penetrate beneath the cut edge. In the sample cut by PL (Fig. 9c), the recast layer was indexed poorly due to the possible oxidation. By investigating the composition of the recast layer using EDX (Fig. 10e, f), it was observed that there is an abundance of oxygen in this area relative to the base material – indicating that oxidation has occurred here during PL machining. Therefore, it can be suggested that for pulsed laser samples, the magnetic deterioration can be reduced through the reduction in recast layer thickness – which has the added effect of lowering the amount of magnetically undesirable oxides. The base material did not undergo any texture transformation. In the sample cut by CW (Fig. 9d), there are no visible gradients at cut edge. This indicates that the stress introduced is homogenous at this observation depth – which is supported by the nanoindentation data. Similar to the PL sample, there is a layer of oxygen in the cut edge of the CW sample, although, in CW this oxidation occurs deeper beneath the cut edge. This could occur due to a greater volume of material becoming molten and interacting with the surrounding atmosphere before re-solidification. Surprisingly, the AWJ sample also shows a layer of oxygen in the cut edge (Fig. 10a, b). However, this only appears on the top of the cut surface, which is most likely due to oxidation which is exacerbated by the high presence of water during cutting, thus the careful drying after cutting would be recommended to reduce the duration that the NOES is exposed.

As discussed when investigating the macro-level features present on the cut surface, and as suggested by prior studies examining annealed samples [35], the stresses induced by machining are thought to play a role in the deterioration of magnetic properties. As the laminations are too thin to undergo residual stress measurement by XRD, the low angle local misorientations (0–5°) have been measured and mapped (Fig. 11) to gain some insight into the stress conditions affecting the laminations.

For the samples cut by AWJ, EDM, and PL, clear regions that are more numerous in low angle local misorientations are observed directly below the cut edges (~1–5°), indicating a highly strained condition in these areas. This strain is expected to locally deform the magnetic domain structure beneath the cut edge, hindering ideal magnetisation by domain wall motion which would present
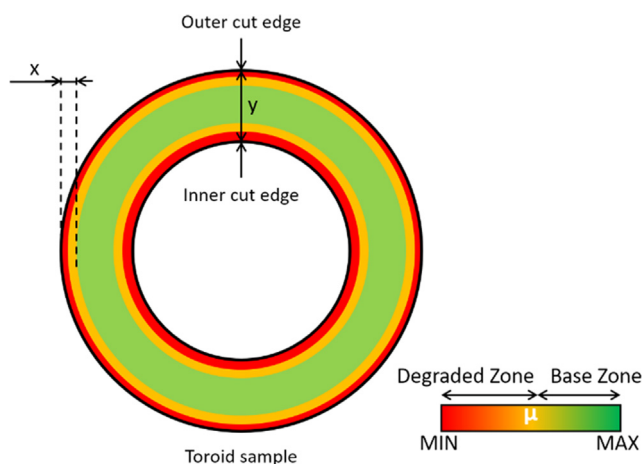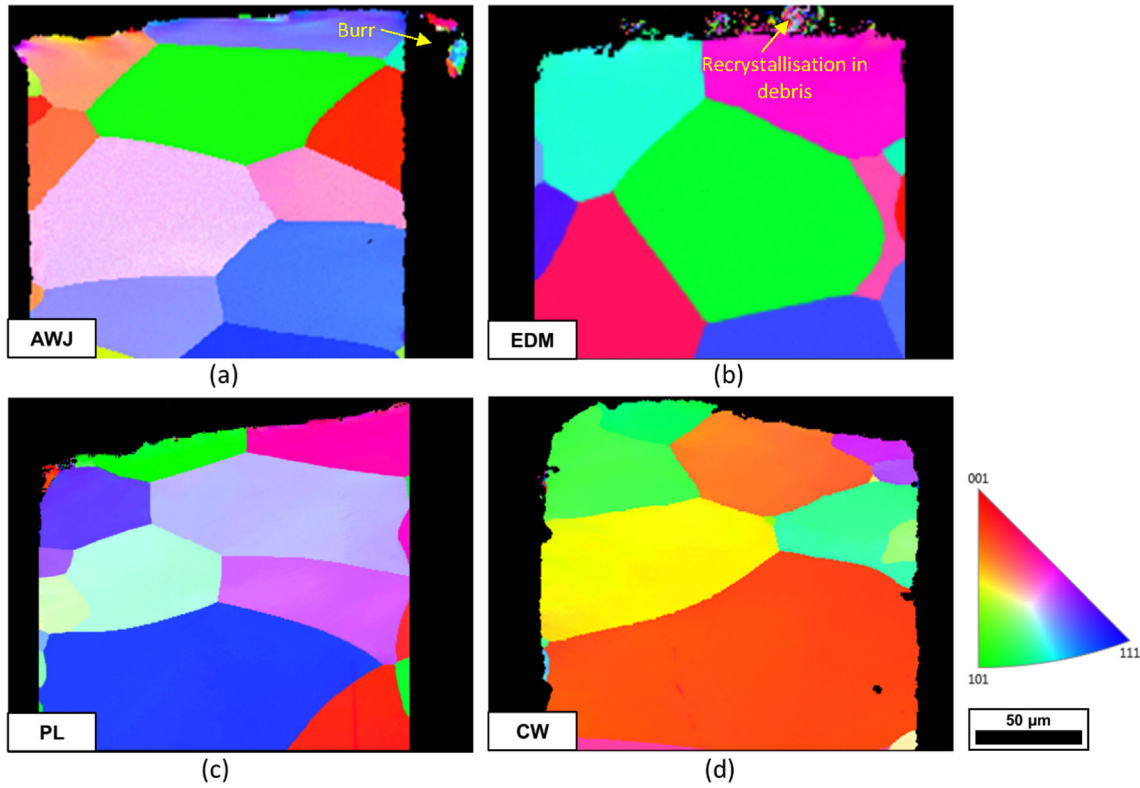
Fig. 9. Normal IPF maps observing the cut edge at a cross-section view for samples machined by abrasive waterjet, wire EDM, pulsed laser, and continuous wave laser – Investigating whether the crystallographic texture has been altered after machining. A noise reduction modifier was applied to all maps to fill small non-measured pixels.
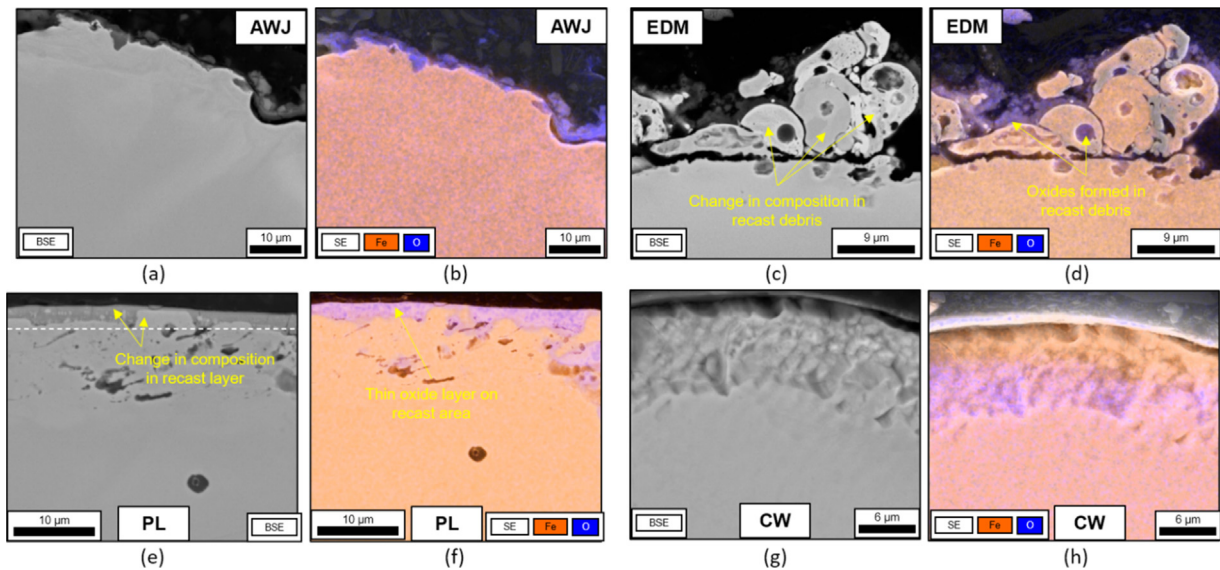
Fig. 10. BSE signal micrographs of the recast layer for samples machined by abrasive waterjet, wire EDM, pulsed laser, and continuous wave laser - where atomic contrast is visible (a, c, e, g), and the corresponding EDX maps coloured to reveal the Oxygen abundance at the cut edge - indicating oxidation (b, d, f, h).

as a decrease in B and an increase in core losses. In the sample cut by AWJ, this was expected due to the mechanical strain hardening that is local to the cut edge. Likewise, in the samples cut by EDM and PL, a level of low angle local misorientations were expected based on the local hardness observed in the nanoindentation results. Surprisingly, an increased level of low angle local misorientations was not observed in the sample cut by CW like the others in the 1–5° data bin. Although, the relative homogeneity of the local misorientations does share similarities with the nanoindentation

data. For the CW laser process, wavy fluctuations in the local misorientations faintly occur in the 0.5° region, suggesting that the thermally induced deformation in the CW sample is within the sub-grain structure and hence, cannot be clearly observed by local misorientation mapping which can only reveal the localised stress conditions.

Therefore, to investigate sub-grain structure in the samples, grain referenced orientation deviation (GROD)-angle maps were produced (Fig. 12). These maps plot the misorientation angle rela-
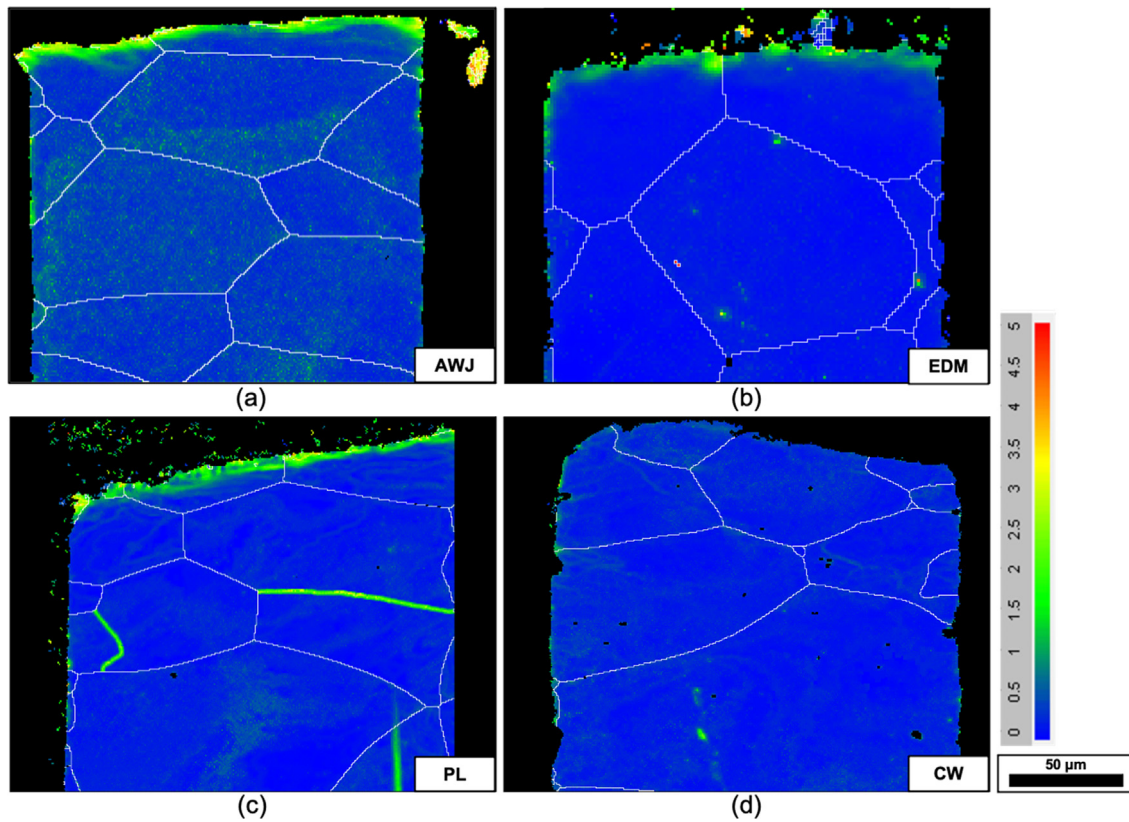
Fig. 11. Local misorientation maps of the subsurface (cross-section view) for samples machined by abrasive waterjet, wire EDM, pulsed laser, and continuous wave laser. Highlighting the localisation of the machining stresses. The grain boundaries are highlighted in white. Noise reduction filters were not applied for these maps to avoid introducing errors in the measurement of local misorientation angle. Non-measured points are coloured black.
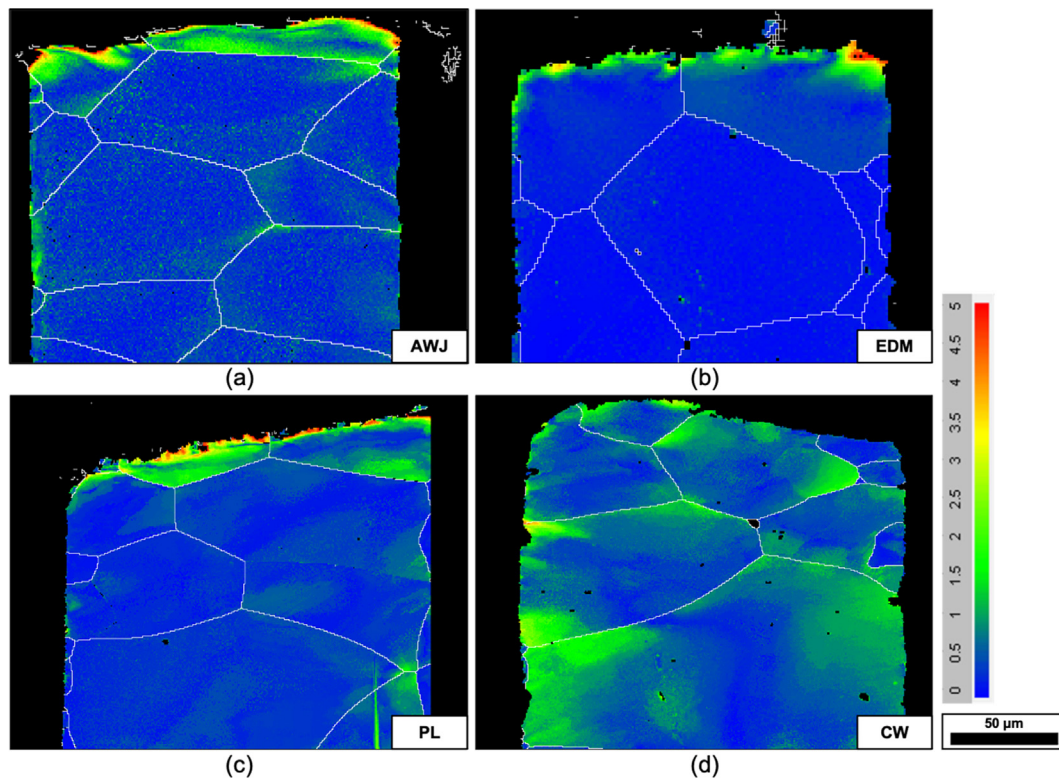
Fig. 12. GROD-angle maps of the subsurface (cross-section view) for samples machined by abrasive waterjet, wire EDM, pulsed laser, and continuous wave laser. Allowing observation of sub-grain structures and how these are influenced by machining stresses. The grain boundaries are highlighted in white. Noise reduction filters were not applied for these maps to avoid introducing errors in the measurement of GROD angle. Non-measured points are coloured black.
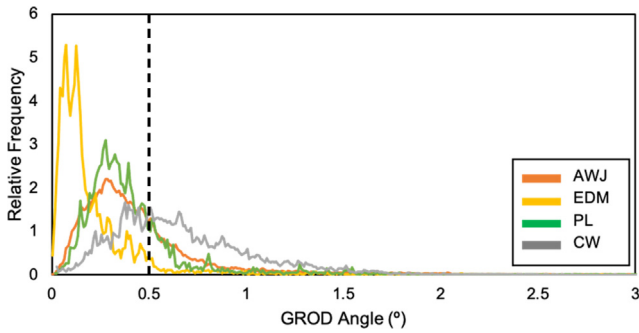
Fig. 13. GROD-angle distribution beneath the subsurface for samples machined by abrasive waterjet, wire EDM, pulsed laser, and continuous wave laser.

Fig. 14. Diagram labelling the "easy" and "hard" axes of magnetisation in a BCC crystal.

tive to the grains' average orientation. This can reveal the low angle misorientations that are characteristic of the induced lattice deformation occurring within the sub-grain structure. Similar to the nanoindentation data, a trend of localisation in the volume of misorientations occurring beneath the cut edge can be observed, decreasing as depth into the workpiece increases. In the sample cut by AWJ (Fig. 12a), it can be observed how the grains directly beneath the cut edge is where the mechanical deformation is occurring. In the samples cut by thermal methods (EDM, PL, CW) (Fig. 12b, c, d), the thermal deformation is reminiscent of a pattern which the turbulent heat flow through the material would be expected to make. That is, in the EDM and PL processes, due to the short pulse duration the heat can be dissipated relatively fast, hence confining the deformation within the superficial layer – minimising the depth that the thermally induced deformation occurs when compared to cutting by CW. In CW, due to the continuous transfer of a high thermal load into the material, there is a high accumulation of heat energy which is dissipated through a

deeper proportion of the thin laminations. Interestingly, the high accumulation of lattice deformation in CW sample appears alongside the grain boundaries, indicating that the transferred heat energy provides the initial strain conditions prior to grain boundary sliding occurring. This can cause a high pinning effect in magnetisation process as the domain walls interact with the lattice deformations – requiring a greater amount of energy to rotate the these to achieve saturation.

For the samples cut by AWJ, EDM, and PL, the misorientations relative to the grain's average that are >1° are concentrated directly beneath the cut edge. This is contrasted in the sample cut by CW where the misorientations relative to the grain's average that are >1° are not concentrated directly beneath the cut edge, rather,
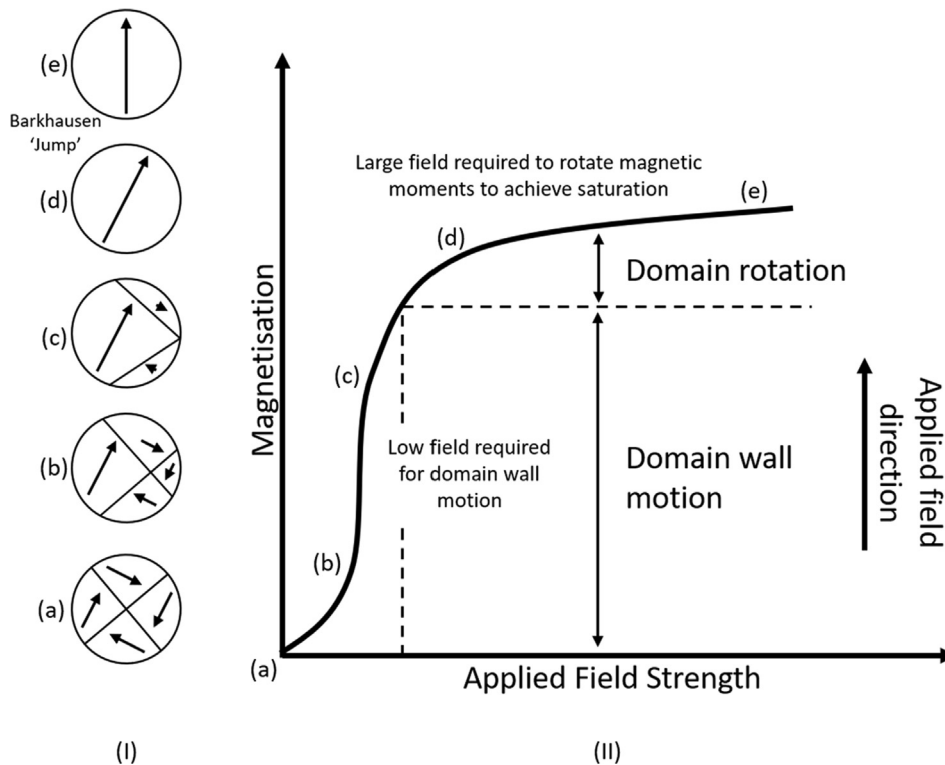
Fig. 15. Diagram of single crystal domain structure through increasing stages of magnetisation (I-a,b,c,d,e) and the corresponding magnetisation curve representation (II) showing the behaviour of the domain structure in the influence of an applied field. (Modified from [3]).
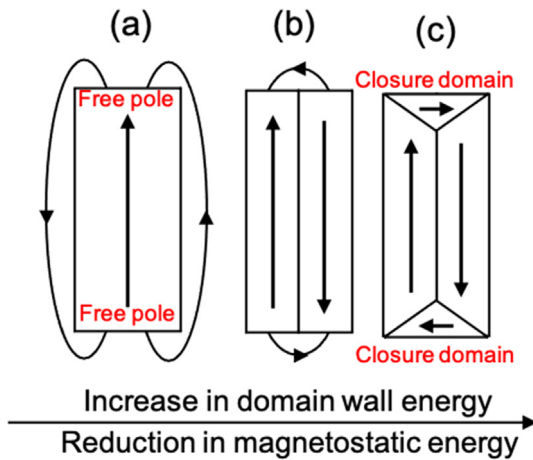
Fig. 16. Diagram of domain structure of a single domain (a), multi-domain (b) and closure domains (c) showing how a material can decrease its' magnetostatic energy at the cost of increasing domain wall energy.

highlights the high localisation of the stresses to the region directly beneath the cut edge. This is closely followed by the samples that are cut by AWJ and PL, where the peak abundance also occurs at very low angle misorientations (<0.5°). On the other hand, the sample cut by CW is less abundant in the <0.5° misorientations than the other methods and is more abundant those >0.5°. This high abundance of >0.5° misorientations occurring throughout a higher proportion of the observed area indicates that lattice deformation, albeit of a relatively low magnitude, is occurring deeper in the material after cutting by CW. Linking this finding with magnetic domain theory, it becomes apparent that even with relatively low angle misorientations the lattice deformation occurring in the sub-grain structure can be high enough to cause interactions with the domain walls – inhibiting the domain wall movement.

3.4. Microscale investigations of the magnetic domain structure at the cut edge

In order to reveal the fundamental mechanisms that govern the extent of microscale magnetic deterioration due to the influence of sub-surface imperfections, i.e., interactions with the domain wall structure, magnetic domain imaging was performed on the cross-sections of each sample from the different machining methods (Figs. 17–20). The index cubes from the grains show the closest easy axes of magnetisation to demonstrate the alignment of the magnetic domain walls. In general, the magnetic domain walls represent the transition between magnetic moments that are rotated

they are distributed deeper throughout the observed area, due to the high level of thermal penetration. By plotting the relative frequency of these grain referenced misorientations (Fig. 13), key information about the scale of the lattice deformation can be determined. For the sample cut by EDM, the relatively high abundance of very low angle misorientations (<0.2°) and low abundance of

Fig. 17. Forward Scatter Detector images observing magnetic contrast for a sample after machining by abrasive waterjet. The whole sample width is imaged (a), the domain structure at the cut edge is imaged (b), the domain structure in the burr is imaged (c), and the domain structure away from the cut edge is imaged with index cubes from the grains showing the closest easy axes of magnetisation to demonstrate the alignment of the domain walls (d).

in different directions. Neighbouring magnetic domains are ideally oriented at 180° to each other and follow an easy axis of magnetisation [3]. The easy axes exist due to magnetocrystalline anisotropy where there is a change in the energy required to magnetise the material depending upon the crystallographic orientation. For example, in a crystal with a body-centred cubic structure (BCC) which is relevant for the α-Fe present in this study, the easy axes occur along the $\langle 1\,0\,0 \rangle$ axes, i.e., the 'x, y, z' directions (Fig. 14). When the magnetic domains are aligned with an easy axis of magnetisation, the magnetocrystalline anisotropy energy is at its' lowest value. Low magnetocrystalline anisotropy is desirable for the soft magnetic materials, i.e., NOES, which form the motor core so that the rotor can become magnetised throughout the full 360° of motion. Hence, by investigating the magnetic domain structure after machining and its' alignment with the axes of magnetisation, it is the first time where an understanding has been gained into the mechanisms by which the lattice deformation interacts with the static magnetic domain structure after machining by different methods. These interactions act to restrict the motion of the magnetic domains in an applied field and thus, they inhibit the propagation of magnetic flux density through the NOES, requiring a greater external field to be applied to achieve magnetic saturation via domain rotation – resulting in higher core losses.

To link the observations from the magnetic domain imaging (Figs. 17–20) with domain theory, the mechanisms that cause the deterioration in magnetic properties should be further understood. From the diagrams of a single crystal domain structure under the influence of an applied field (Fig. 15I), the mechanism of domain wall motion occurs at low field strengths so that the net magnetisation vector acts in one direction that is at an angle to the applied field direction (Fig. 15I,II-a, b, c, d) [3]. In order for saturation to be achieved, i.e., further magnetisation, work must be done against the anisotropy force through domain rotation by increasing the applied field strength [36], this aligns the net magnetisation of the crystal with the applied field direction near instantaneously (Barkhausen jump) (Fig. 15I-d, e). Work done against the anisotropy force is realised as losses, and so it becomes apparent how it is desirable for magnetisation to occur through a greater proportion of domain wall motion.

The domain structure in the material after machining can subsequently be used to understand magnetic deterioration mechanisms. As observed in the local misorientation (Fig. 11) and GROD mapping (Fig. 12), deformation is introduced during machining to varying extents. These deformations increase the magnetic free pole density in the domain structure (Fig. 16a), which increases the magnetostatic energy. In order to reduce this

(a)

(b)

(c)
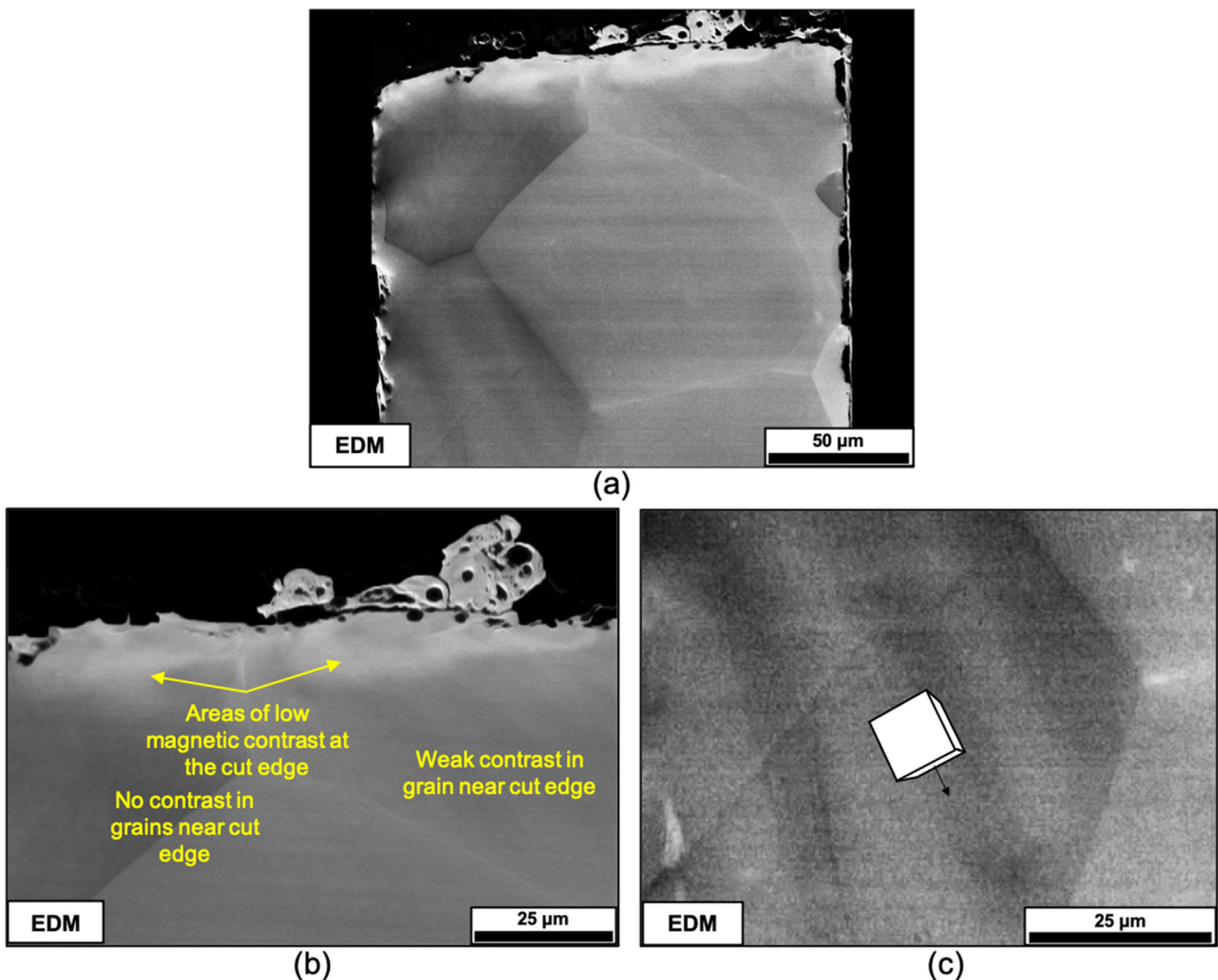
Fig. 18. Forward Scatter Detector images observing magnetic contrast for a sample after machining by wire EDM. The whole sample width is imaged (a), the magnetic contrast at the cut edge is imaged (b), and the domain structure away from the cut edge is imaged with an index cube from a grain showing the closest easy axis of magnetisation to demonstrate the alignment of the domain walls (c).

magnetostatic energy, 180° domain walls (Fig. 16b) form that reduce the domain area but increase the total length of domain walls – increasing the domain wall energy. To further reduce the magnetostatic energy and achieve a demagnetised state, closure domains (90° domain walls) form (Fig. 16c). This leads to a further increase in domain wall energy. By comparing this with the domain imaging (Figs. 17–20), a reduction in domain size was observed in the areas with higher deformation in AWJ (Fig. 17). An increase in the disorder of the domain structure was also observed near the cut edge, which would act to reduce magnetisation through domain wall motion. Although the NOES has intrinsic magnetic anisotropy, a proportion of stress-induced anisotropy would remain present after cutting, causing the domains to energetically favour the easy axis that is closest to the mechanical stress direction. For the thermal machining methods (e.g., EDM, PL and CW (Figs. 18–20)), a decrease in the magnetic contrast is observed near the cutting edge as opposed to the disordered domains. This could imply that the domains have been reduced in size and are not visible at the current magnification, or more probable, that there is an increased proportion of closure domains in these areas – limiting the observable magnetic domain contrast for the imaging method. In this case, an abundance of closure

domains could explain an increase in domain wall energy, further limiting the magnetisation through domain wall motion and subsequently occurring through domain wall rotation.

For the sample cut by AWJ (Fig. 17), the domains become more disordered at the cut edge (Fig. 17b). The areas such as the entry point and the burr (Fig. 17c), which undergo a large amount of mechanical stress, have a reduced domain wall size and do not follow an easy axis of magnetisation. More interestingly, at the entry point, the domains appear to follow a stress contour caused by the impingement of abrasive material, as shown in Fig. 12. This is due to the lattice distortion with a high dislocation density that acts as an obstacle – impeding the domain from remaining in a low-energy state, causing the domain structure to distort in order to maintain its' low magnetocrystalline anisotropy energy. Domains further away from the edge (Fig. 17d) that are less affected by the effects of machining have wider, striped domains that align with an easy axis of magnetisation. It should be noted that in the regions where a higher proportion of mechanically induced deformation occurs (i.e., along the cut edge (Fig. 17b) and within the burr (Fig. 17c)), that the magnetic domain contrast may be partially masked by electron channelling contrast. However, the large scattering angle (70°) and increased accelerating voltage (30 kV)
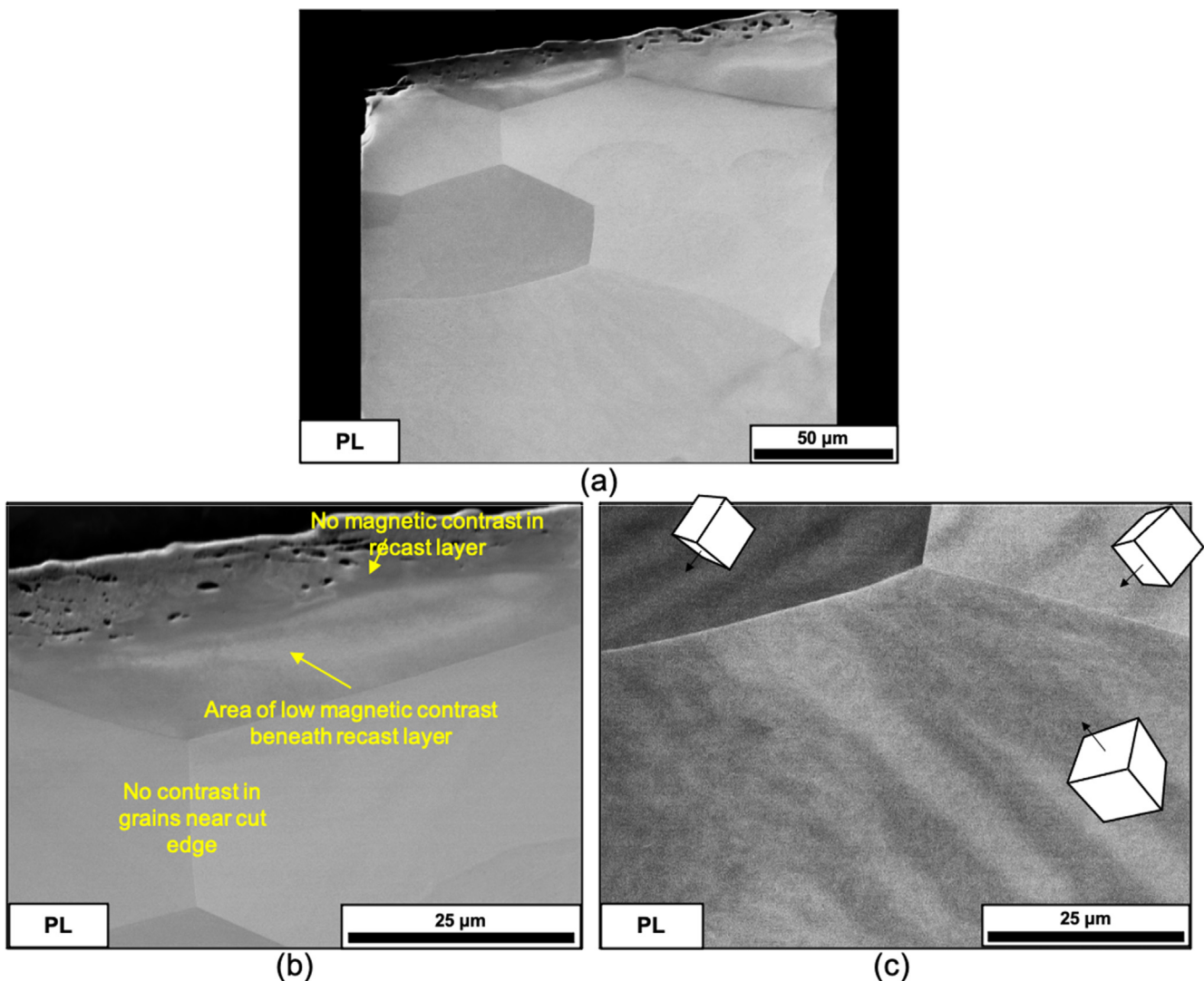
Fig. 19. Forward Scatter Detector images observing magnetic contrast for a sample after machining by pulsed laser. The whole sample width is imaged (a), the domain structure at the cut edge is imaged, showing the low magnetic contrast near the cut edge and no magnetic contrast in the recast layer (b), and the domain structure away from the cut edge is imaged with index cubes from the grains showing the closest easy axes of magnetisation to demonstrate the alignment of the domain walls (c).

for imaging with the FSD has been found to increase the magnetic contrast within electrical steels [39], providing support to the claim that the distorted structures arise from magnetic interactions as is observed in the material further away from the cut edge.

For the sample cut by EDM (Fig. 18), there is little magnetic contrast directly below the cut edge (Fig. 18b). In a grain further away from the cut edge where there is less deformation observed (Fig. 18c), the magnetic contrast is increased, and the domains are wider and more ordered. The low magnetic contrast is evidence of distortion of the domain walls. This suggests that during machining, the deformation introduced causes an increase in free pole density which increases the magnetostatic energy. The domain structure then divides and distorts to decrease its' magnetostatic energy to maintain a demagnetised state. This offers the mechanism by which the magnetic deterioration occurs – where the lower domain contrast represents the reduced proportion of domains that are aligned with an easy axis of magnetisation, requiring more work done to align the magnetic moments in these domains with an applied field.

For the sample cut by PL (Fig. 19), there is no magnetic contrast in the recast layer (Fig. 19a). This confirms that recast layer thickness is a key factor when decreasing the amount of magnetic deterioration that occurs after cutting with PL. There is also little magnetic contrast in the grains directly below the cut edge of the sample cut with PL – similar to the low contrast observed in

EDM. As this effect cannot be attributed to changes in the previously investigated crystallographic texture, this low contrast is recognised to be influenced by residual tensile stresses causing deformations in the sub-grain structure (demonstrated by the previous misorientation mapping) which interact with the domain walls. Deeper beneath the cut edge, ordered domains with an easy axis alignment have been observed (Fig. 19c).

For the sample cut by CW (Fig. 20), there is no magnetic contrast directly below the cut edge (Fig. 20b). The surrounding grains have weak magnetic contrast, and in these weak contrast areas, the domains are disordered and offer no alignment with an easy axis of magnetisation. Therefore, near the cut edge, as the domains aren't aligned with an easy axis, more work is required for the magnetic moments to rotate to become aligned with an applied field. Deeper beneath the cut edge, the more desirable, ordered domains that are aligned with an easy axis of magnetisation are observed (Fig. 20c). As with the other thermal processes (PL, EDM), it can be suggested that the reduced contrast near the cut edge is due to deformations in the sub-grain structure (caused by the thermal tensile stress) which increase the free pole density at the surface, causing 90° closure domains to form in order to maintain a low magnetostatic energy. To address the order observed in the initial magnetic deterioration experiment, after cutting with CW, the deformations act deeper into the material due to the high power and intensity of the laser used. This is supported by the nanoindentation data
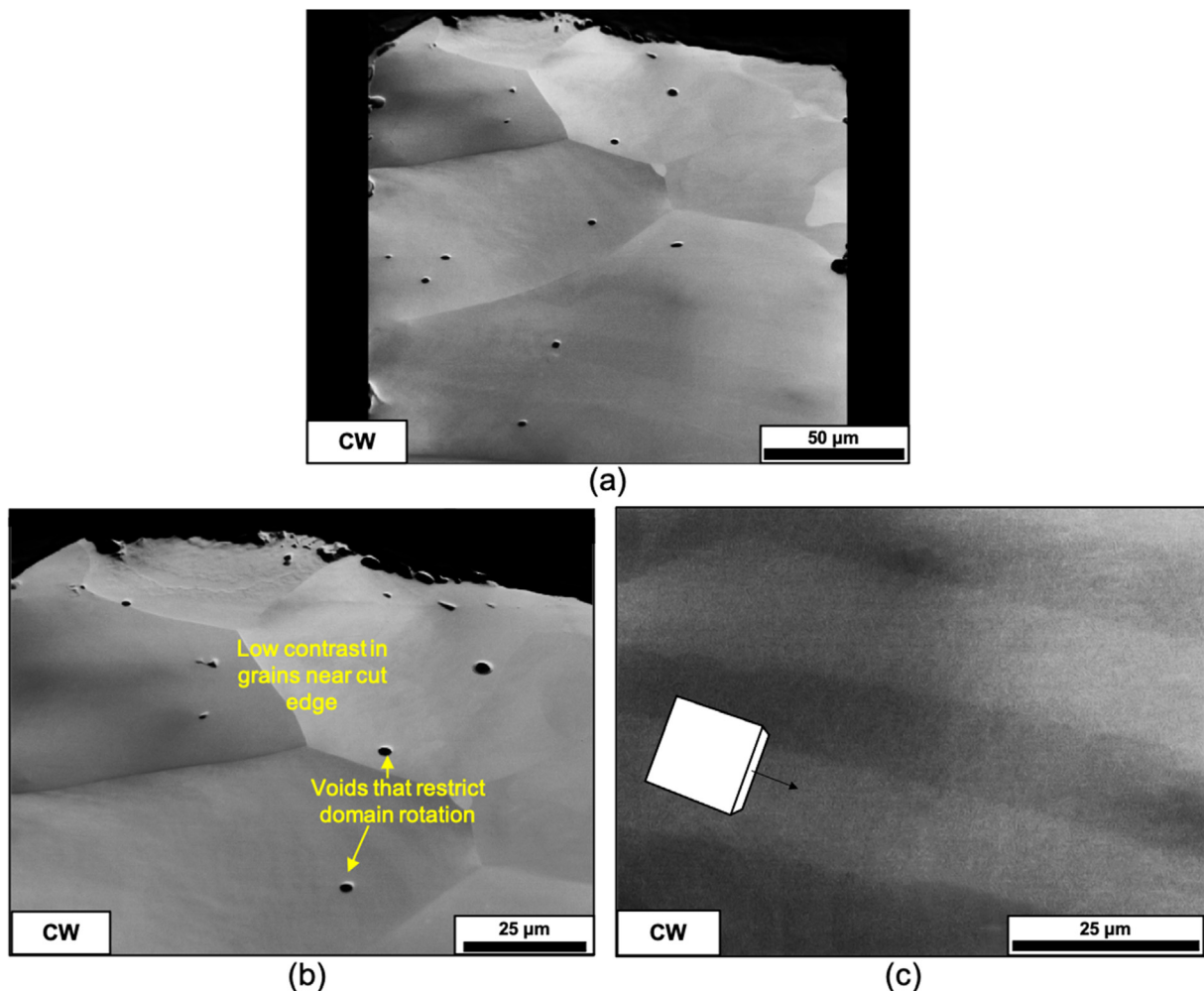
Fig. 20. Forward Scatter Detector images observing magnetic contrast for a sample after machining by continuous wave laser. The whole sample width is imaged (a), the domain structure at the cut edge is imaged, showing the low magnetic contrast near the cut edge (b), and the domain structure away from the cut edge is imaged with an index cube from a grain showing the closest easy axis of magnetisation to demonstrate the alignment of the domain walls (c).
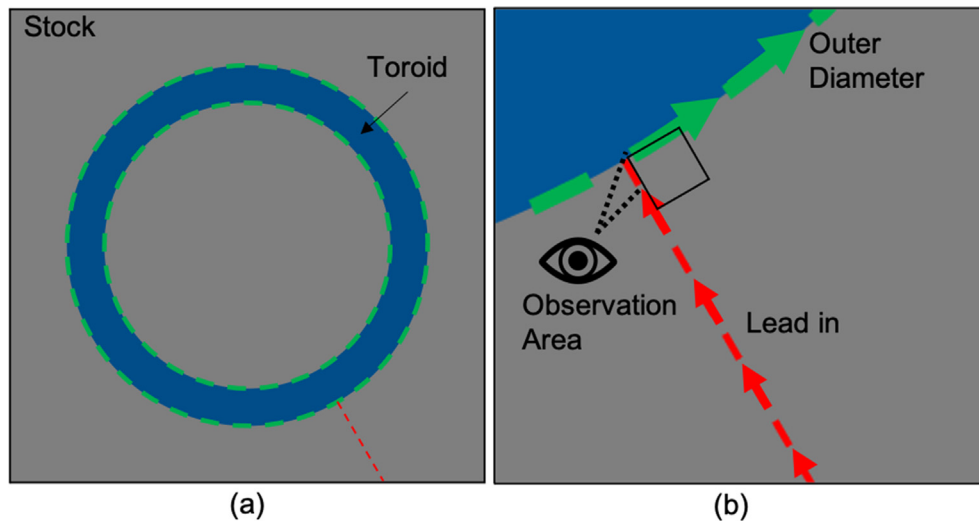
Fig. 21. Diagram representing the top view for machining the 'corner' sample by wire EDM (a) with a magnified view (b) showing the radial relationship of the lead in and outer diameter of the toroid, highlighting the observation area.
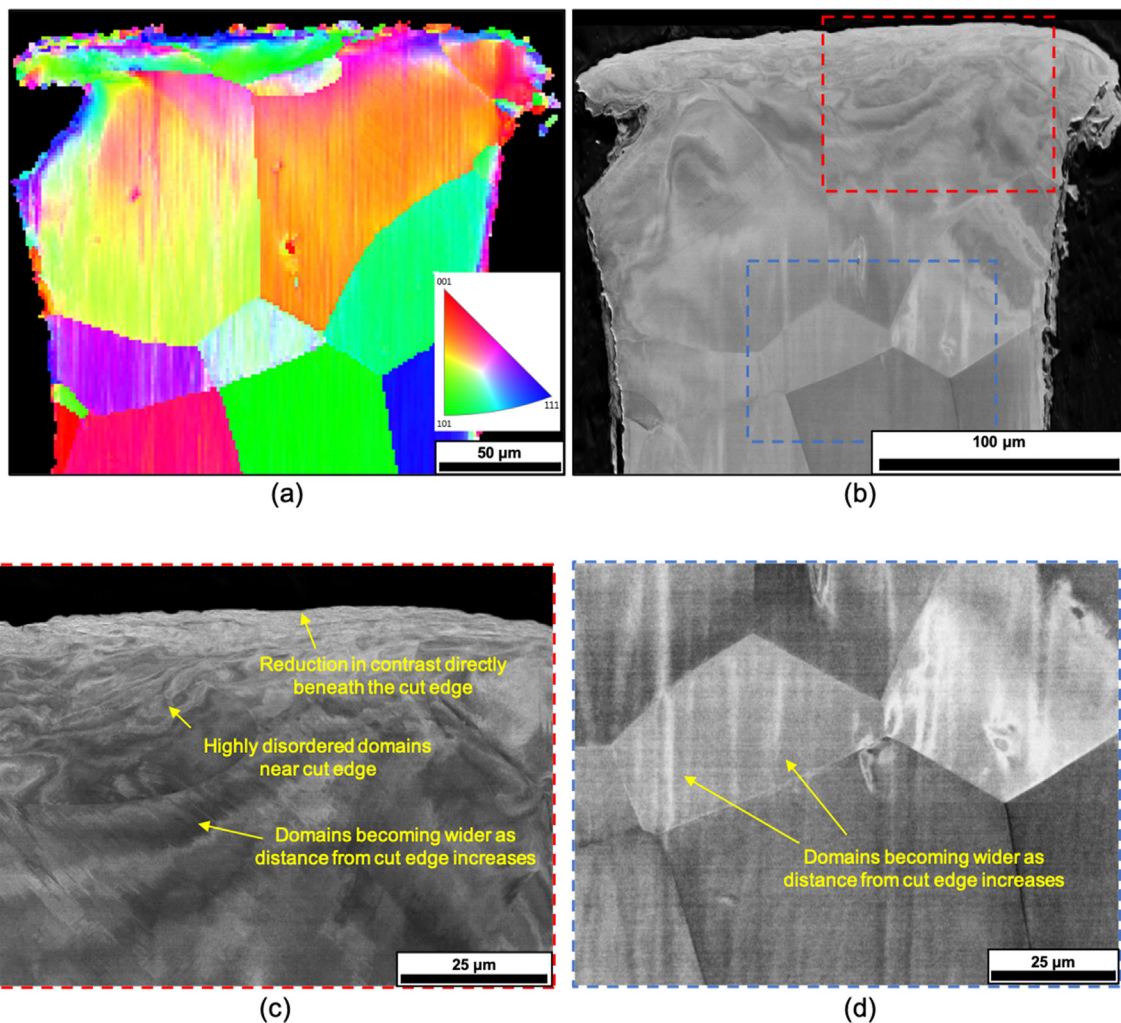
Fig. 22. Normal Inverse Pole Figure map (a), Forward Scatter Detector magnetic domain image (b), with magnification of an area immediately beneath the cut edge (c), and with magnification of an area away from the cut edge (d), for the corner of a sample machined by wire EDM.

which highlights the low level of localisation in the CW process. Moreover, many magnetic voids have been observed which act deep into the material. It is unclear whether these voids are intrinsic to the material, are induced by machining, or an artefact from sample preparation. Nevertheless, these not-only will reduce the total availability of magnetic domains for alignment – limiting maximum saturation, they will also act as pinning sites, inhibiting the domain wall motion in an applied magnetic field – which would increase the energy required for the domain walls to become aligned, thus, increasing core losses.

More interestingly, in an EDM 'corner' sample, which is comprised of the lead-in intersecting the outer diameter of the toroidal sample radially (Fig. 21), the domain wall structure appears to be highly distorted near to the cut edge (Fig. 22b, c). This is in contrast with the domain wall structure further beneath the cut edge (Fig. 22b, d) where the surface domains appear to be unidirectional, regardless of the crystallographic orientations found within the grains. As this paper investigates the toroidal sample whereby only the influence of one cut edge is the focus, it was observed that there is a significant increase in magnetic domain deformation when multiple cut edges in close proximity are influencing the observation area. This has a correlation with the decreased stability of the crystallographic texture within individual grains (Fig. 22a) which indicates that the corners experience a significantly greater amount of deformation than the single cut edges. The practical relevance of this finding is that motor cores are rarely designed with geometry as simple as a toroid, rather, they incorporate a multitude of slots. These slots act to increase the total length of cut edge in the sample, thus, compounding the effects that induced lattice deformations have on the magnetic domain structure. Therefore, when cutting a design consisting of many edges and corners, a further investigation of their influence needs to be considered. In the beam-based processes, e.g., AWJ and laser, there is no cutting tool (e.g., wire) used, hence, no such effect was observed and can be preferential for machining intricate lamination geometries.

4. Conclusion

In this paper, non-oriented electrical steel (NOES) sheets have been machined by a variety of non-conventional machining methods. After machining the samples were characterised magnetically to determine an order of performance. The selection of machining method used to cut core laminations of non-oriented electrical steel has a strong influence on the level of deterioration of the magnetic performance. By comparing standard surface integrity analyses with imaging of the magnetic domains, the mechanisms behind the deterioration have been proposed. This is, that an increase in deformation depth caused by the machining stresses leads to an increase in interactions with the domain structure (walls). This increases the free pole density in the material and so the magnetic domains divide to reduce the magnetostatic energy to a demagnetised state. This increase in total magnetic domain wall length causes an increase in wall energy which opposes the magnetisation in an applied field, yielding greater losses and lower achievable saturation values. The main findings of the paper can be summarised as follows:

- The most desirable magnetisation curves with the highest saturation at the lowest applied field strength is achieved through AWJ machining, which also shows the lowest core losses. Machining by EDM and PL results in similar magnetic performance which both show higher losses, and lower saturation magnetisation than machining by AWJ. The least desirable magnetisation curves with exceptionally lower saturation and very high core losses occurred in the sample which was machined by CW.

- The topography of the cut surface present after machining operations was measured by optical profilometry. There was correlation with the order of magnetic deterioration and the areal surface roughness (S_a), but this does not reveal causation, rather, it provides macro-level insights into the types of stresses present based on the surface features that are characteristic of each machining method. For AWJ, these are scratches which can influence the magnetic domains by introducing compressive residual stresses into the NOES. For PL, these are a recast layer with microcracks beneath and directional a bias which introduces a magnetically hardened region, leading to increased coercivity. For EDM, this is a mottled surface with no directional bias unlike the beam methods which allows for high geometrical accuracy of the cut. For CW, the surface is coated with resolidified material that is ejected in a backwards flow and blown back into the cutting site – with a high directional bias which may lead to shorting when stacking the laminations and increase the Eddy losses.

- EBSD misorientation mapping has suggested that the introduction of machining stresses causes lattice deformation within the sub-grain structure which interacts with domain motion. Whilst the AWJ, PL, and EDM samples all experienced misorientations local to the cut edge, the misorientations were much more ubiquitous in sample cut by the high-power CW laser. Therefore, many more stress induced pinning points were present for restricting domain motion.

- The influence that the machining of NOES has on the micromagnetic structure was studied by imaging the magnetic domains. Proposed regions of disordered and shrunken magnetic domains have been observed near the cut edge. These observations allow for comparisons to be made based on magnetic domain theory, leading to explanations behind the fundamental mechanisms causing changes in the magnetic properties of the NOES that are induced by cutting operations. Stresses are known to increase the free-pole density at the surface, and on interaction with these stresses, the magnetic domain walls become disordered and reduce in size to reduce the magnetostatic energy in the demagnetised state. Magnetic domains imaged away from the cut edge for all processes have been found to be wider and aligned with one of the easy axes of magnetisation.

CRediT authorship contribution statement

Kieran Winter: Writing – original draft, Conceptualization, Investigation. **Zhirong Liao:** Conceptualization, Investigation, Writing – review & editing, Supervision, Funding acquisition. **Ramkumar Ramanathan:** Investigation, Writing – review & editing. **Dragos Axinte:** Conceptualization, Supervision, Funding acquisition. **Gaurang Vakil:** Investigation. **Christopher Gerada:** Conceptualization, Supervision, Funding acquisition.

Declaration of Competing Interest

The authors declare that they have no known competing financial interests or personal relationships that could have appeared to influence the work reported in this paper.

Acknowledgement

References

[1] Flightpath 2050, Europe's vision for aviation : maintaining global leadership and serving society's needs, Publications Office, Luxembourg: Luxembourg, 2012.

[2] T.J.E. Miller, Brushless permanent-magnet and reluctance motor drives, Clarendon Press, Oxford: Oxford, 1989.

[3] B.D. Cullity, C.D. Graham, Introduction to Magnetic Materials, second ed., John Wiley & Sons, Inc., Hoboken, NJ, USA, 2008.

[4] Andreas Krings, Aldo Boglietti, Andrea Cavagnino, Steve Sprague, Soft Magnetic Material Status and Trends in Electric Machines, IEEE Trans. Ind. Electron. 64 (3) (2017) 2405–2414.

[5] D. Petrovic, Non-Oriented Electrical Steel Sheets, Materiali In Tehnologije 44 (6) (2010) 317–325.

[6] Y. Zhang, R. Kang, Z. Dong, Q. Wang, X. Zhu, R. Xu, D. Guo, Microstructural Evolution of Soft Magnetic 49Fe-49Co-2V Alloy Induced by Drilling, Mater. Des. 189 (2020) 108501. Web.

[7] Ahmed Al-Timimy, Gaurang Vakil, Michele Degano, Paolo Giangrande, Chris Gerada, Michael Galea, Considerations on the Effects That Core Material Machining Has on an Electrical Machines Performance, IEEE Trans. Energy Convers. 33 (3) (2018) 1154–1163.

[8] M. Mieszala, P.L. Torrubia, D.A. Axinte, J.J. Schwiedrzik, Y. Guo, S. Mischler, J. Michler, L. Philippe, Erosion Mechanisms during Abrasive Waterjet Machining: Model Microstructures and Single Particle Experiments, J. Mater. Process. Technol. 247 (2017) 92–102. Web.

[9] Dun Liu, Thai Nguyen, Jun Wang, Chuanzhen Huang, Mechanisms of enhancing the machining performance in micro abrasive waterjet drilling of hard and brittle materials by vibration assistance, Int. J. Mach. Tools Manuf 151 (2020) 103528, https://doi.org/10.1016/j.ijmachtools.2020.103528.

[10] Priyaranjan Sharma, D. Chakradhar, S. Narendranath, Evaluation of WEDM Performance Characteristics of Inconel 706 for Turbine Disk Application, Mater. Des. 88 (2015) 558–566. Web.

[11] Guodong Li, Wataru Natsu, Zuyuan Yu, Study on quantitative estimation of bubble behavior in micro hole drilling with EDM, Int. J. Mach. Tools Manuf 146 (2019) 103437, https://doi.org/10.1016/j.ijmachtools.2019.103437.

[12] Dirk Herzog, Matthias Schmidt-Lehr, Max Oberlander, Marten Canisius, Markus Radek, Claus Emmelmann, Laser Cutting of Carbon Fibre Reinforced Plastics of High Thickness, Mater. Des. 92 (2016) 742–749. Web.

[13] D. Cha, D. Axinte, J. Billingham, Geometrical modelling of pulsed laser ablation of high performance metallic alloys, Int. J. Mach. Tools Manuf 141 (2019) 78–88.

[14] Takeshi Omura, Yoshiaki Zaizen, Masaru Fukumura, Kunihiro Senda, Hiroaki Toda, Effect of Hardness and Thickness of Nonoriented Electrical Steel Sheets on Iron Loss Deterioration by Shearing Process, IEEE Trans. Magn. 51 (11) (2015) 1–4.

[15] H.M.S. Harstick, M. Ritter, A. Plath, W. Riehemann, EBSD Investigations on Cutting Edges of Non-Oriented Electrical Steel, Metallogr. Microstruct. Anal. 3 (4) (2014) 244–251.

[16] Y.Z. Liu, Coaxial waterjet-assisted laser drilling of film cooling holes in turbine blades, Int. J. Mach. Tools Manuf 150 (2020) 103510, https://doi.org/10.1016/j.ijmachtools.2019.103510.

[17] Madeleine Bali, Annette Muetze, The Degradation Depth of Non-grain Oriented Electrical Steel Sheets of Electric Machines Due to Mechanical and Laser Cutting: A State-of-the-Art Review, IEEE Trans. Ind. Appl. 55 (1) (2019) 366–375.

[18] Zhirong Liao, Ali Abdelhafeez, Haonan Li, Yue Yang, Oriol Gavalda Diaz, Dragos Axinte, State-of-the-art of surface integrity in machining of metal matrix composites, Int. J. Mach. Tools Manuf 143 (2019) 63–91.

[19] Oriol Gavalda Diaz, Gonzalo Garcia Luna, Zhirong Liao, Dragos Axinte, The new challenges of machining Ceramic Matrix Composites (CMCs): Review of surface integrity, Int. J. Mach. Tools Manuf 139 (2019) 24–36.

[20] A Belhadj, P Baudouin, Y Houbaert, Simulation of the HAZ and magnetic properties of laser cut non-oriented electrical steels, J. Magn. Magn. Mater. 248 (1) (2002) 34–44.

[21] D. Xu, Z. Liao, D. Axinte, J.A. Sarasua, R. M'Saoubi, A. Wretland, Investigation of Surface Integrity in Laser-assisted Machining of Nickel Based Superalloy, Mater. Des. 194 (2020) 108851. Web.

[22] O. Perevertov, Influence of the applied elastic tensile and compressive stress on the hysteresis curves of Fe-3%Si non-oriented steel, J. Magn. Magn. Mater. 428 (2017) 223–228.

[23] Mattia Bellotti, Jun Qian, Dominiek Reynaerts, Breakthrough phenomena in drilling micro holes by EDM, Int. J. Mach. Tools Manuf 146 (2019) 103436, https://doi.org/10.1016/j.ijmachtools.2019.103436.

[24] Vinod Yadav, Vijay K. Jain, Prakash M. Dixit, Thermal stresses due to electrical discharge machining, Int. J. Mach. Tools Manuf 42 (8) (2002) 877–888.

[25] M. Kantha Babu, O.V. Krishnaiah Chetty, Studies on Recharging of Abrasives in Abrasive Water Jet Machining, Int. J. Adv. Manuf. Technol. 19 (9) (2002) 697–703.

[26] Henrike M.S. Harstick, Martin Ritter, Werner Riehemann, Influence of Punching and Tool Wear on the Magnetic Properties of Nonoriented Electrical Steel, IEEE Trans. Magn. 50 (4) (2014) 1–4.

[27] Zhirong Liao, Irati Sanchez, Dongdong Xu, Dragos Axinte, Giedrius Augustinavicius, Anders Wretland, Dual-processing by abrasive waterjet machining—A method for machining and surface modification of nickel-based superalloy, J. Mater. Process. Technol. 285 (2020) 116768, https://doi.org/10.1016/j.jmatprotec.2020.116768.

[28] F. Boud, C. Carpenter, J. Folkes, P.H. Shipway, Abrasive waterjet cutting of a titanium alloy: The influence of abrasive morphology and mechanical properties on workpiece grit embedment and cut quality, J. Mater. Process. Tech 210 (15) (2010) 2197–2205.

[29] A Schoppa, H Louis, F Pude, Ch von Rad, Influence of abrasive waterjet cutting on the magnetic properties of non-oriented electrical steels, J. Magn. Magn. Mater. 254-255 (2003) 370–372.

[30] Anon, BS 6404-4:1986, IEC 60404-4:1982: Magnetic materials. Methods of measurement of the d.c. magnetic properties of solid steels, 1986.

[31] Matthew Gallaugher, Nicolas Brodusch, Raynald Gauvin, Richard R. Chromik, Magnetic domain structure and crystallographic orientation of electrical steels revealed by a forescatter detector and electron backscatter diffraction, Ultramicroscopy 142 (2014) 40–49.

[32] D.J. Fathers, J.P. Jakubovics, D.C. Joy, D.E. Newbury, H. Yakowitz, A new method of observing magnetic domains by scanning electron microscopy. II. Experimental confirmation of the theory of image contrast, Phys. Stat. 22 (2) (1974) 609–619.

[33] W.C. Oliver, G.M. Pharr, An improved technique for determining hardness and elastic modulus using load and displacement sensing indentation experiments, J. Mater. Res. 7 (6) (1992) 1564–1583.

[34] D.K. Shanmugam, J. Wang, H. Liu, Minimisation of kerf tapers in abrasive waterjet machining of alumina ceramics using a compensation technique, Int. J. Mach. Tools Manuf. 48 (14) (2008) 1527–1534.

[35] Wenmin Shi, Jing Liu, Changyi Li, Effect of Cutting Techniques on the Structure and Magnetic Properties of a High-grade Non-oriented Electrical Steel, J. Wuhan Univ. Technol. Mater. Sci. Ed. 29 (6) (2014) 1246–1251.

[36] D.C. Jiles, Dynamics of domain magnetization and the Barkhausen effect, Czech J. Phys. 50 (8) (2000) 893–924.

[37] H. Ilker Yelbay, Ibrahim Cam, C. Hakan Gür, Non-destructive determination of residual stress state in steel weldments by Magnetic Barkhausen Noise technique, NDT E Int. Indep. Nondestruct. Test. Eval. 43 (1) (2010) 29–33.

[38] Dongdong Xu, Zhirong Liao, Dragos Axinte, A novel method to continuously map the surface integrity and cutting mechanism transition in various cutting conditions, Int. J. Mach. Tools Manuf 151 (2020) 103529, https://doi.org/10.1016/j.ijmachtools.2020.103529.

[39] T. Yamamoto, H. Nishizawa, K. Tsuno, High voltage scanning electron microscopy for observing magnetic domains, J. Phys. D, Appl. Phys. 8 (9) (1975) L113–L114, https://doi.org/10.1088/0022-3727/8/9/001.